



Review

## Recent progress in nickel based materials for high performance pseudocapacitor electrodes



Liangdong Feng <sup>a,b,c</sup> <sup>\*\*</sup>, Yufu Zhu <sup>b,c</sup>, Hongyan Ding <sup>b,c</sup>, Chaoying Ni <sup>b,\*</sup>

<sup>a</sup> Key Laboratory for Palygorskite Science and Applied Technology of Jiangsu Province, Department of Chemical Engineering, Huaiyin Institute of Technology, Huai'an, 223003, PR China

<sup>b</sup> Department of Materials Science and Engineering, University of Delaware, Newark, DE 19716, USA

<sup>c</sup> Jiangsu Provincial Key Laboratory for Interventional Medical Devices, Department of Mechanical Engineering, Huaiyin Institute of Technology, Huai'an, 223003, PR China

### HIGHLIGHTS

- Nickel based materials for high performance pseudocapacitor electrodes were reviewed.
- Strategies adopted to improve the electrical conductivity of nickel based materials were assessed in details.
- The energy density and power density of some recent nickel based materials were summarized and discussed.
- Perspectives as to the future directions of nickel based materials were provided.

### ARTICLE INFO

#### Article history:

Received 12 January 2014

Received in revised form

10 May 2014

Accepted 17 May 2014

Available online 13 June 2014

#### Keywords:

Nickel oxide

Nickel hydroxide

High performance

Pseudocapacitor

Hybrid materials

### ABSTRACT

Nickel based materials have been intensively investigated and considered as good potential electrode materials for pseudocapacitors due to their high theoretical specific capacity values, high chemical and thermal stability, ready availability, environmentally benign nature and lower cost. This review firstly examines recent progress in nickel oxides or nickel hydroxides for high performance pseudocapacitor electrodes. The advances of hybrid electrodes are then assessed to include hybrid systems of nickel based materials with compounds such as carbonaceous materials, metal and transition metal oxides or hydroxides, in which various strategies have been adopted to improve the electrical conductivity of nickel oxides or hydroxides. Furthermore, the energy density and power density of some recently reported NiO, nickel based composites and NiCo<sub>2</sub>O<sub>4</sub> are summarized and discussed. Finally, we provide some perspectives as to the future directions of this intriguing field.

© 2014 Elsevier B.V. All rights reserved.

### 1. Introduction

Because of the increasing demands for energy and the growing concerns about air pollution and global warming, one of modern day grand challenges is to provide environmentally friendly, cost-effective and robust energy resources [1–8]. Among various energy storage systems, supercapacitors, also known as ultracapacitors or electrochemical capacitors, have been considered as one of the most promising energy-storage and energy management devices due to their higher power density ( $D_p$ ) with better cycling lifespan than batteries and higher energy density ( $D_e$ ) than conventional capacitors [8,9]. Based on charge storage mechanisms

and active materials utilized, supercapacitors can be classified into two types: electric double layer capacitors (EDLCs) and pseudocapacitors [2–4]. The capacity of EDLCs comes from pure electrostatic charges accumulated at the interface of electrode/electrolyte. The pseudocapacitors typically show higher capacities owing to the fast and reversible faradic redox reactions of electro-active materials of the electrodes, and the  $D_e$  of pseudocapacitors is usually many times greater than that of the EDLCs [10–16]. Fig. 1 shows a simplified Ragone plot of  $D_p$  versus  $D_e$  for some electrochemical energy storage devices [17,18]. As shown in Fig. 1, the  $D_e$  value of supercapacitors is about one magnitude lower than that of batteries, which has hindered their wider application in the field of energy storage. It is an ongoing challenge to develop supercapacitors that can deliver high energy density, and recent studies have shown that high energy density is possible for actual storage technologies [17].

\* Corresponding author. Fax: +1 302 831 4545.

\*\* Corresponding author. Key Laboratory for Palygorskite Science and Applied Technology of Jiangsu Province, Department of Chemical Engineering, Huaiyin Institute of Technology, Huai'an 223003, PR China. Fax: +86 517 839 1019.

In general, parameters such as capacity, voltage, power density and energy density were adopted to evaluate a supercapacitor. The capacity of a supercapacitor cell is half of either electrode's capacity in symmetric supercapacitor or is limited by the electrode with smaller capacity in an asymmetric supercapacitor. The value of a supercapacitor's voltage is dependent on the electrodes' materials and electrolyte used. The theoretical  $D_e$  and  $D_p$  of the supercapacitor can be expressed as Equations (1) and (2) [19,20]:

$$D_e = \frac{1}{2} CV^2 \quad (1)$$

$$D_p = \frac{V^2}{4R_s} \quad (2)$$

where  $V$  is the voltage (in volts) of the supercapacitor,  $C$  is the total capacity of the supercapacitor (in farads) and  $R_s$  is the equivalent series resistance (in ohms) of the supercapacitor. The capacity of the supercapacitor depends extensively upon the electrode material.  $R_s$  comes from various types of resistance associated with the intrinsic electronic properties of the electrode, electrolyte solution, mass transfer resistance of ions in the electrode, and contact resistance between the current collector and the electrode [20]. Hence, it is obvious that the development of electrode materials with high performance is one of the crucial criteria to optimize the performance of a supercapacitor.

Specific capacity ( $C_s$ ) is often adopted to evaluate an electrode material for supercapacitors, with a unit of  $\text{F g}^{-1}$  (Faraday per gram). The  $C_s$  of a material is usually tested in a three electrode system, the material acts as working electrode and the counter electrode is oversized than working electrode. So, the measured capacity is dominated by the working electrode. Average  $C_s$  values can be determined from the cyclic voltammometric curves as follows [21,22]:

$$C_s = \frac{\int I dt}{m \Delta V} \quad (3)$$

where  $I$  is the oxidation/reduction current,  $dt$  is the time differential,  $m$  is the mass of the active electrode material, and  $\Delta V$  is the voltage range of one scanning segment. The  $C_s$  values can also be determined from the cyclic chronopotentiometric curves as follows [21,22]:

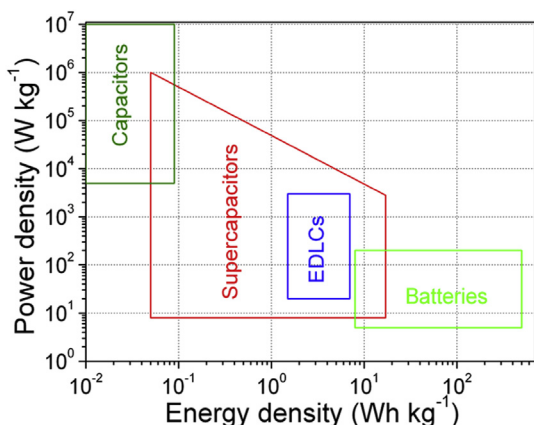


**Fig. 1.** A simplified Ragone plot of  $D_p$  versus  $D_e$  for some electrochemical energy storage devices.

$$C_s = \frac{I \times \Delta t}{m \times \Delta V} \quad (4)$$

where  $I$  is the charge/discharge current,  $\Delta t$  is the duration for a full charge or discharge,  $m$  is the mass of the active material, and  $\Delta V$  is the voltage change after a full charge or discharge.

In literature, authors often adopt  $D_e$  and  $D_p$  to evaluate the performance of electrodes' materials. And they can be calculated from the cyclic voltammetric or cyclic chronopotentiometric curves as follows [21,22]:

$$D_e = \frac{1}{2} C_s (\Delta V)^2 \quad (5)$$

$$D_p = \frac{D_e}{\Delta t} = \frac{C_s (\Delta V)^2}{2 \Delta t} \quad (6)$$

where  $\Delta V$  and  $\Delta t$  represent the voltage change after a full charge or discharge and the duration for a full charge or discharge in cyclic chronopotentiometric test, or represent scan voltage and the time for a scan segment in a cyclic voltammetric test, respectively. From Equations (5) and (6), the  $D_e$  and  $D_p$  can be increased by increasing the values of  $C_s$  and  $\Delta V$ , and both  $D_e$  and  $D_p$  are proportional to the square of  $\Delta V$ . Although increasing  $\Delta V$  is apparently more effective than increasing  $C_s$  for the purpose of achieving high  $D_e$  and/or  $D_p$ , for some applications, however, one cannot increase or change the potential range since redox reactions occur only at certain potential or the electrolyte limits the potential range. The pseudocapacitive materials are usually applied in aqueous solution, and the voltage windows are generally as low as about 1.2 V with few exceeding 1.5 V [23], which is much lower than those of organic electrolytes [24]. Therefore, it is of special significance at present to improve the  $C_s$  value so as to achieve desirable  $D_e$  and  $D_p$ .

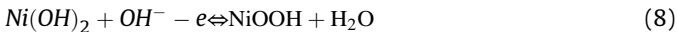
Various materials have been investigated for applications as the electrodes in supercapacitors, including carbonaceous materials, transition metal oxides or hydroxides, and conducting polymers [25–27]. Although carbon materials have many advantages such as higher specific surface area, good electronic conductivity, and high chemical stability, but the low  $C_s$  value greatly limits their further applications [28]. In most cases, the measured  $C_s$  values of carbon materials in real supercapacitors are in the range of 75–175  $\text{F g}^{-1}$  for aqueous electrolytes and 40–100  $\text{F g}^{-1}$  for organic electrolytes [19], which is lower than that of transition metal oxides or hydroxides. Transition metal oxides or hydroxides not only store charges via an electrical double layer mechanism, but also undergo fast and reversible surface redox reactions, and their  $C_s$  values may be 10–100 times greater than those of conventional carbon materials. Among metal oxides/hydroxides,  $\text{RuO}_2$  has been widely researched because of its superior electrochemical properties such as high proton conductivity and a highly reversible redox process [29,30]. However, its practical applicability is impeded by its toxicity, high costs and naturally less abundance of the initial materials. Compared to  $\text{RuO}_2$ , nickel-based materials, in particular, nickel hydroxide ( $\text{Ni(OH)}_2$ ) and nickel oxide ( $\text{NiO}$ ), have attracted extra interests due to their high theoretical  $C_s$  values (the theoretical  $C_s$  values of  $\text{NiO}$  and  $\text{Ni(OH)}_2$  in a potential window of 0.5 V are 2584 and 2082  $\text{F g}^{-1}$ , respectively), high chemical and thermal stability, ready availability, environmentally benign nature and lower cost [31–36]. In 1996, Liu and Anderson for the first time used porous  $\text{NiO}$  as a possible electrode material for supercapacitor applications, and the measured  $C_s$  value was about 50–60  $\text{F g}^{-1}$  [37]. In order to further increase the  $C_s$  of nickel-based materials, synthesis of nanosized nickel-based materials with novel morphologies, hierarchical porous structures, large pore volume and high specific surface area has been attempted by various methods.

Although the maximum  $C_s$  value of some reported nickel-based materials could reach more than  $2000 \text{ F g}^{-1}$ , but there still exist several major drawbacks, such as their relatively low conductivity, which leads to the problem of bad rate capability and long time charge/discharge cycling instability. In addition to a high  $C_s$  value, a high performance pseudocapacitor electrode material should also possess good redox reversibility and stability. More importantly, the internal resistance must be low enough to obtain high rate capability during charge/discharge process. In order to further improve the performance of nickel-based materials, combining them with other compounds is one of the most commonly used constructions for electrochemical capacitors.

In this review, a summary is first made of important factors influencing the pseudocapacitance of nickel-based materials. Recent strategies are then discussed on improving the performance of nickel based pseudocapacitor electrode materials. Based on the consideration of applications, the  $D_e$  and  $D_p$  values of recently reported  $\text{NiO}$ , nickel based composites and  $\text{NiCo}_2\text{O}_4$  are evaluated and compared. Finally, we provide some perspectives as to the future directions of this intriguing field and several possible research trends in nickel based materials for high performance pseudocapacitors.

## 2. Factors influencing the pseudocapacitive performance of nickel-based materials

The performance of nickel based pseudocapacitor electrode materials is determined by the redox reaction of nickel oxide or hydroxide in an alkaline electrolyte, and can be expressed as Equation (7) or (8) [37]:



The pseudocapacitance of nickel-based materials is influenced by material parameters, such as the structure, conductivity and crystallinity, electrolyte, and material loading mass on the electrode.

### 2.1. Structure

The  $C_s$  of electrode materials can be greatly influenced by their structure including morphology, size, specific surface area, pore size and distribution. The morphology is closely related to the specific surface area, but there have been few systematic studies on the unique morphology-dependent supercapacitance properties against the surface characteristics. Primarily because not all of the surface area is electrochemically accessible by the electrolyte, the measured  $C_s$  is not a linear function of the specific surface area. The porosity relevant to the development of high capacity is itself not a simple parameter, involving both pore sizes and pore-size distribution for a given overall specific area of the material. According to Lu et al., the size, geometry, length, alignment of pores and the degree of pore ordering will all influence the performance of supercapacitors [38]. Therefore, the capacity strongly depends on the surface area of the electrode accessible to the electrolyte. However, very little work has yet been done in systematically studying the principles for optimizing electrode architectures, especially those involving redox reactions.

### 2.2. Conductivity

Another important factor is the conductivity of electrode materials. When at a high charge/discharge rate, the resistance

to electron conduction will be more pronounced in a material with low electrical conductivity, and the charge/discharge processes can only be localized in a finite volume near the current collector, the  $C_s$  value will be dropped sharply and low conductivity electrode materials will restrict their high-power applications [38].

### 2.3. Crystallinity

In a pseudocapacitor, electrode materials with low crystallinity have high density of the grain boundaries with fine grains, leading to more efficient diffusion channels for electrolyte ions. Low crystallinity materials can therefore enhance the utilization of materials and exhibit larger  $C_s$  than their high crystallinity counterparts [38,39].

### 2.4. Electrolyte

The pseudocapacitive materials are usually employed in aqueous solution. Aqueous electrolytes can provide a higher ionic concentration and lower resistance than organic electrolytes. Due to higher ionic concentration and smaller ionic radius, electrochemical supercapacitors with aqueous electrolyte may display higher capacity and higher power than those with organic electrolytes. Unfortunately, a large disadvantage of aqueous electrolytes is their small voltage window of as low as about 1.2 V, much lower than those of organic electrolytes. Based on Equations (5) and (6), the aqueous electrolytes have a large limitation in terms of improving both energy and power density. The concentration of electrolyte can influence the performance of pseudocapacitors, too. For example, Wang et al. measured the electrochemical impedance spectra of  $\text{Co}_3\text{O}_4$  nanowires in 1, 2, 4, and  $6 \text{ mol L}^{-1}$  KOH aqueous solution, and demonstrates that all of the Warburg resistance, the charge transfer resistance and the internal resistance decrease with increasing concentration of KOH [40]. Here, the Warburg resistance reflects the diffusion of redox species in the electrolyte, the charge transfer resistance results from the diffusion of electrons, and the internal resistance includes the inherent resistance of the electro active material, bulk resistance of electrolyte, and contact resistance at the interface between electrolyte and electrode. If the concentration was lower than  $0.01 \text{ mol L}^{-1}$ , owing to the lower concentration of ions participating in the redox reactions, the performance of pseudocapacitance materials was decreased [41]. Usually, the electrolyte used in nickel based materials is KOH or NaOH with a concentration varying from about  $0.5 \text{ mol L}^{-1}$  to  $6 \text{ mol L}^{-1}$ . However, there appears to have few studies on the relationship between the concentration of electrolyte and the pseudocapacitance of nickel based materials.

### 2.5. Loading mass

For practical applications, both high  $C_s$  value and large mass loading of active materials are needed for the reason of applying high power and energy. However, in most of the reported literatures about nickel based pseudocapacitive materials, the mass loading of the active material was less than  $10 \text{ mg cm}^{-2}$ . In general, the  $C_s$  value decreases with increased mass loading. Because large mass loading may produce disadvantages such as lower electronic conductivity, difficult accessing of the electrolyte to all of the active surfaces and higher series resistance due to longer transport paths for the diffusion of protons. As a result, both  $C_s$  value and rate capability can be reduced.

### 3. Recent progress in improving the pseudocapacitance performance of NiO or Ni(OH)<sub>2</sub> materials

#### 3.1. Increasing $C_s$ values via controlling its construction

##### 3.1.1. Morphology and particle size

The morphology and particle size of electrode materials can exert a wide influence over the speed of ion transfer and the ability related to electrolyte wetting. Thereby, NiO or Ni(OH)<sub>2</sub> with different morphology and size such as one-dimensional (1D) (e.g. nanotubes or nanowires), two-dimensional (2D) (nanoplatelets or nanosheets) and three-dimensional (3D) cross-linked materials have been fabricated and their capacitive properties have been investigated by different electrochemical methods.

In supercapacitors, owing to reduced contact resistance, electrodes constructed with oriented 1D nanostructure arrays are expected to facilitate the charge/discharge kinetics and show better charge transport ability [42]. Even with the same dimension, NiO with different morphology and size may have different  $C_s$  values. For instance, NiO arrays with slim (<20 nm) rod morphology on Ni foam showed ultrahigh  $C_s$  value of 2018 F g<sup>-1</sup> at 2.27 A g<sup>-1</sup> (or 5 mA cm<sup>-2</sup>), as shown in Fig. 2a and b, and the high  $C_s$  value could be attributed to the slim morphology, high crystallinity, regularly aligned array structure and strong bonding of the nanorods to the metallic Ni substrate [43]. In contrast, disordered mesoporous nickel oxide nanowires with diameters of 40–60 nm and lengths extending a few tens micrometers exhibited a  $C_s$  value of 348 F g<sup>-1</sup> at a scan rate of 20 mV s<sup>-1</sup> [44].

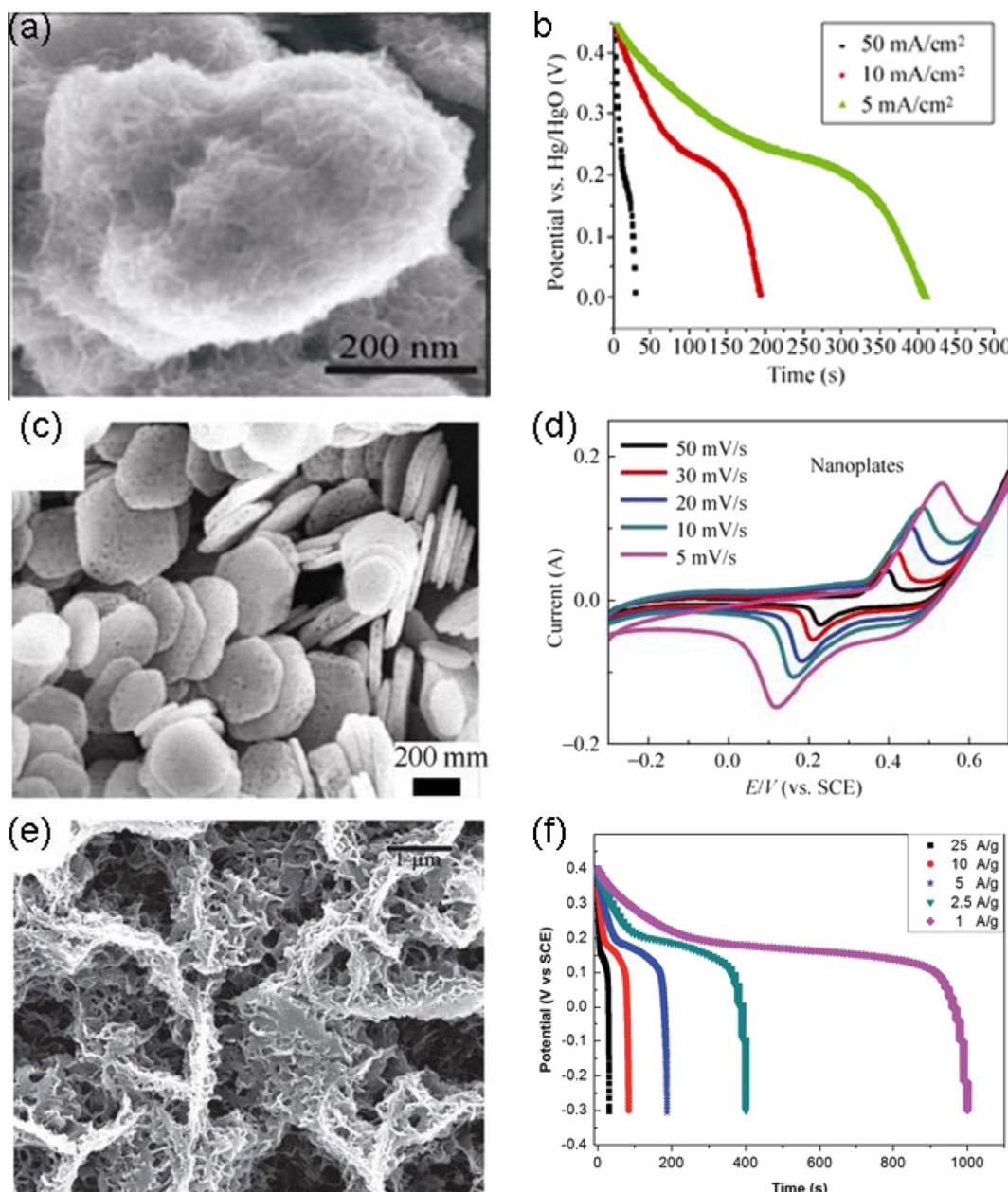


**Fig. 2.** Morphologies and discharging curves at different current densities of 1D NiO arrays (a and b); SEM image and cyclic voltammograms of 2D NiO nanoplates (c and d); SEM image and discharging curves at different current densities of 3D nanoporous NiO film (e and f). (a) & (b) reprinted with permission from Ref. [43]. Copyright 2011, Springer; (c) & (d) reprinted with permission from ref 35. Copyright 2010, Springer; (e) & (f) reprinted with permission from Ref. [47]. Copyright 2012, American Chemical Society Royal Society of Chemistry.

The reported 2D NiO nanostructures such as stacking of triangular prisms and nanoflake showed relatively low  $C_s$  value of 232 and  $401 \text{ F g}^{-1}$  [45,46], respectively. Fig. 2c and d presented the morphology of porous NiO nanoplates and its cyclic voltammograms in  $1 \text{ mol L}^{-1}$  KOH aqueous solution with different scan rates, and the  $C_s$  value at  $5 \text{ A g}^{-1}$  could reach to  $285 \text{ F g}^{-1}$  [35].

Most of the 3D nanostructured NiO are formed from cross-linked nanoflakes or nanowires, and their  $C_s$  values are in the range of  $300\text{--}1800 \text{ F g}^{-1}$  [47–49]. The difference in  $C_s$  values may be rooted in the thickness or diameter of the nanoflakes or nanowires. Such as, the  $C_s$  value of a 3D nanoporous NiO film composed of cross-linked nanoflakes with a size distribution of  $3 \text{ nm}\text{--}8 \text{ nm}$  was  $1790 \text{ F g}^{-1}$  at a discharge current density of  $2.5 \text{ A g}^{-1}$  (as shown in Fig. 2e and f) [47]. And mesoporous NiO network-like hierarchical microspheres, based on the topotactic transformation from  $\alpha\text{-Ni(OH)}_2$ , exhibited a  $C_s$  value of  $555 \text{ F g}^{-1}$  at  $2 \text{ A g}^{-1}$  [48]. In addition, porous nickel oxide microflowers composed of small NiO nanoparticles with  $20\text{--}30 \text{ nm}$  could present a  $C_s$  value of  $1678 \text{ F g}^{-1}$  at a current density of  $0.625 \text{ A g}^{-1}$  [50].

To explore the relationship between the morphology of NiO and its  $C_s$  values, Zhang et al. prepared different morphologies of NiO and proved that the  $C_s$  value of the porous NiO nanocolumns ( $390 \text{ F g}^{-1}$ ) was significantly higher than that of the nanoslices ( $176 \text{ F g}^{-1}$ ) or nanoplates ( $285 \text{ F g}^{-1}$ ) at a discharge current of  $5 \text{ A g}^{-1}$ , which showed a structure-dependence in their specific charge capacities [35]. The adequate pores in NiO nanocolumns provide effective diffusion channels for the electrolyte ions. In particular, such porous nanostructures can act as “ion-buffering reservoirs” to sustain the supply of  $\text{OH}^-$  ions and ensure continuous occurring of sufficient Faradic reactions at high current densities. Very recently, Kim et al. also synthesized NiO nanostructures with three distinct morphologies (nanoflower, nanoslice and nanoparticle, respectively) and studied their morphology-dependent capacity properties [51]. They discovered that the nanoflower shaped NiO with a distinctive 3D network and the highest porosity showed the best pseudocapacitor properties, and the nanopores in flower shaped nanostructures had the advantages in contact with and transport of the electrolyte and allowed for 3D nanochannels in NiO structure for longer electron pathways.

It has been determined that  $\text{Ni(OH)}_2$  can yield much higher  $C_s$  values than NiO [52]. For example, pompon-like mesoporous  $\alpha\text{-Ni(OH)}_2$  nanosphere could present a maximum  $C_s$  value of  $1718 \text{ F g}^{-1}$  at a scan rate of  $5 \text{ mV s}^{-1}$  [53]. The  $C_s$  values of porous nanostructured  $\alpha\text{-Ni(OH)}_2$  film electrode, prepared through selective anodic dissolution of copper from an electrodeposited Ni–Cu alloy film and following cathodic electrodeposition, were  $1634$ ,  $1563$  and  $1512 \text{ F g}^{-1}$  at current densities of  $2$ ,  $5$  and  $10 \text{ A g}^{-1}$ , respectively [54]. In addition to  $\alpha\text{-Ni(OH)}_2$ , Lv et al. synthesized nanostructured plate-like  $\beta\text{-Ni(OH)}_2$  on nickel foam substrate via a mild hydrothermal process [55]. The plate, composed of a stack of highly closely packed nanoflakes with the thickness of about  $20 \text{ nm}$ , were approximately perpendicular to the surface of the substrate with several ones grouped together, and the thickness of a single nanoplate is in the range of  $145\text{--}250 \text{ nm}$ . This nanostructured  $\beta\text{-Ni(OH)}_2$  displayed a maximum  $C_s$  value of  $1778 \text{ F g}^{-1}$  at a current density of  $2.5 \text{ A g}^{-1}$ , relating to the effective utilization of the unique  $\text{Ni(OH)}_2$  structure.

From the above results, it is clear that although morphologies and particle sizes of NiO or  $\text{Ni(OH)}_2$  are related to materials surface area and the structure for ions or electron transporting paths, these factors only affect the  $C_s$  values to a certain extent. The  $C_s$  value appears to result from the interplay of morphology, particle size, surface area and pore properties of the material.

### 3.1.2. Surface area and pore properties

Large surface area and appropriate pore channel are beneficial for both the accessibility of electrolytes to electrochemically active sites and fast diffusion within redox phases, thus leading to high  $C_s$  values [33,56]. Generally, the  $C_s$  value of a metal oxide increases notably with an increase in its surface area, because a large surface area is associated with more Faradic active sites and in turn higher pseudocapacitance. For example, the unique nano-sheet geometry of NiO with intrinsically high surface area of  $394 \text{ m}^2 \text{ g}^{-1}$  had a  $C_s$  value of  $1025 \text{ F g}^{-1}$ , which was attributed to the high surface area and the small crystal size [57]. In another study, the narrow pore size distribution of  $16 \text{ nm}$  and large surface area of  $349 \text{ m}^2 \text{ g}^{-1}$  of mesoporous  $\alpha\text{-Ni(OH)}_2$  exhibited a higher  $C_s$  value of  $1718 \text{ F g}^{-1}$  [53]. However, in a study by Xia et al. [36], a porous NiO nanoflake network with a specific surface area of  $290 \text{ m}^2 \text{ g}^{-1}$  only showed a  $C_s$  value of  $309 \text{ F g}^{-1}$  at  $1 \text{ A g}^{-1}$ . That indicates that electrode-electrolyte interfaces are not all active. Therefore, increasing the surface area of NiO or  $\text{Ni(OH)}_2$  electrodes does not necessarily guarantee improved performance.

Some reported experimental results have proved that a proper pore structure is an important criterion for the improvement of  $C_s$  values, because the ion diffusion process is always entangled with complicated redox reactions and the driving force of the diffusion process is primarily related to the difference in chemical potential caused by the concentration gradient, which is the same as in nanostructured EDLC-type electrodes [38]. It appears that NiO or  $\text{Ni(OH)}_2$  with mesopores of  $3\text{--}10 \text{ nm}$  in diameter has high  $C_s$  values. The nano-pores  $<2 \text{ nm}$  will restrict the electrolyte entering into the interior of materials resulting in a limited utility of electrode materials. However, mesopores  $>10 \text{ nm}$  increase the average ion travel distance between the pore wall and the center, leading to a decreased  $C_s$ . In addition to the pore size distribution, pore configuration can also greatly influence the  $C_s$  value. For example, owing to a single modal narrow pore-size distribution centered at  $3.7 \text{ nm}$ , NiO electrode materials with uniform slit-structured mesopores presented high  $C_s$  value of over  $1700 \text{ F g}^{-1}$  at a constant current of  $2 \text{ A g}^{-1}$  [58]. Nevertheless, the  $C_s$  value of flowerlike NiO hollow nanospheres with surface area of  $176 \text{ m}^2 \text{ g}^{-1}$  and a narrow pore size distribution centered at  $4 \text{ nm}$  was only  $770 \text{ F g}^{-1}$  at a discharge current of  $5 \text{ A g}^{-1}$  [59]. Therefore, other pore characteristics such as the channel length and ordering of the pores should be considered in investigating the correlation of porosity and  $C_s$  value of nickel based materials.

**Table 1** summarizes the data recently reported in the literature about the structure morphology and size, surface area, pore size, electrolyte,  $C_s$  values, rate capability and stability of synthesized nickel oxides or hydroxides. While the data in this table clearly demonstrate the importance of tailoring the material structure including phase morphology, feature size, surface area, pore size and its distribution for desired electrode performance, there is still a lack of consistent establishment of the correlation among the electrode materials, architectures, and reactions, especially when redox reactions are involved.

### 3.2. Improving the conductivity of NiO or $\text{Ni(OH)}_2$ materials through forming composites

Despite the progress in enhancing the  $C_s$  value of nickel oxides or hydroxides through fabricating materials with different morphologies, sizes, surface areas and pore size distributions, single-phase NiO or  $\text{Ni(OH)}_2$  electrodes are found to have unsatisfactory performances because of their intrinsic weaker material properties in conductivity, cycling stability and mechanical stability [28]. To form NiO or  $\text{Ni(OH)}_2$  composites with conductive components such as carbonaceous materials, metals, transition metal oxides, or

**Table 1**Structural parameters and capacitance properties of some recent published results of NiO and Ni(OH)<sub>2</sub>.

Material and morphology	Size <sup>a</sup>	Surface area (m <sup>2</sup> g <sup>-1</sup> )	Pore size (nm)	Electrolyte	Maximum Cs (F g <sup>-1</sup> ) <sup>b</sup>	Rate capability (F g <sup>-1</sup> ) <sup>b</sup>	Stability <sup>c</sup>	Reference
NiO nanocolumns		102.4		1 mol L <sup>-1</sup> KOH	686 (1)	390 (5)	100% (1000-5)	[35]
NiO porous net-like nanoflakes	~30 nm (T)	290		1 mol L <sup>-1</sup> KOH	309 (1)	221 (40)	89% (4000-1)	[36]
NiO nanorods	<20 nm			1 mol L <sup>-1</sup> NaOH	2018 (2.27)	1536 (22.7)	92% (500-22.7)	[43]
NiO triangular platelets	100 nm (T)	196.8	33–42	1 mol L <sup>-1</sup> KOH	232 (2)	200 (20)	348 F g <sup>-1</sup> (4000-2)	[45]
NiO network-like hierarchical microspheres	3–4 μm (D)	215.3	3.2	6 mol L <sup>-1</sup> KOH	555 (2)	390 (10)	100% (2000-10)	[48]
NiO porous microflowers	10 μm	62.7	5–10	~0.5 mol L <sup>-1</sup> KOH	1678 (0.625)	856 (6.25)	99.7% (1000-6.25)	[50]
NiO nanoflowers		159	16.7	2 mol L <sup>-1</sup> KOH	480 (0.5)	252 (5)		[51]
NiO porous nano/micro sphere		216	64.3	6 mol L <sup>-1</sup> KOH	710 (1)	525 (4)	98% (2000-4)	[56]
NiO porous nanosheets		394	3–4	6 mol L <sup>-1</sup> KOH	1025 (3)	332 (15)	98.2% (500-15)	[57]
Stacked NiO flakes	50–100 nm (D)	259	3.7	6 mol L <sup>-1</sup> KOH	1758 (2)			[58]
NiO flowerlike hollow sphere	300 nm (D)	176	4.0	2 mol L <sup>-1</sup> KOH	770 (2)	320 (10)	95% (1000-5)	[59]
Ni(OH) <sub>2</sub> pompon-like sphere	<1 μm	349	16		1718 (5 mV s <sup>-1</sup> )	1080 (13.9)	~100% (1000)	[53]
Ni(OH) <sub>2</sub> porous film				1 mol L <sup>-1</sup> KOH	1634 (2)	1512 (10)	59.3% (500-10)	[54]
Ni(OH) <sub>2</sub> plate-like	20 nm (T)			2 mol L <sup>-1</sup> KOH	1778 (2.5)	471 (10)		[55]

<sup>a</sup> D = diameter, T = thickness, L = length.<sup>b</sup> Cs value was measured at a discharging current density with unit of A g<sup>-1</sup> in the brackets.<sup>c</sup> Stability means the percentage that the Cs value retained after a number of charge/discharge circles (the first number in the brackets) at a certain current density with unit of A g<sup>-1</sup> (the second number in the brackets).

hydroxides is desired for composite electrodes with synergistically optimized performances.

### 3.2.1. Carbonaceous materials incorporated nickel oxide or hydroxide

Graphene is a two-dimensional nanomaterial with high surface area and good electrical conductivity. When mixed with transition metal oxides or hydroxides, graphene enhances the electrical conductivities and electrochemical activities of the composite [60,61]. For example, when NiO nanoparticles were decorated on graphene sheets, the Cs value of mesoporous graphene/NiO at 2 A g<sup>-1</sup> remained at about 60.6% compared to that at 0.2 A g<sup>-1</sup>, which was contributed to the intrinsic high electronic conductivity of graphene to guarantee prompt electron diffusion in the composite [62]. Significantly, due to the electrochemical-activity reinforcement of the graphene sheet film, a nickel-foam supported graphene sheet/porous NiO hybrid film exhibited outstanding pseudocapacitive behavior with Cs values of 400 and 324 F g<sup>-1</sup> at 2 A g<sup>-1</sup> and 40 A g<sup>-1</sup> respectively [63]. Wang et al. prepared single-crystalline Ni(OH)<sub>2</sub> hexagonal nanoplates directly grown on lightly oxidized, electrically conducting graphene sheets by a two-step method [14]. As shown in Fig. 3a, small β-Ni(OH)<sub>2</sub> nanoparticles were coated on the graphene sheets. A high Cs value of about 1335 F g<sup>-1</sup> was measured at a charge/discharge current density of 2.8 A g<sup>-1</sup> and retained at about 953 F g<sup>-1</sup> at 45.7 A g<sup>-1</sup> (Fig. 3b). Importantly, the columbic efficiency was nearly 100% for each cycle of charge/discharge and there was no obvious Cs decrease observed over 2000 cycles at a high current density of 28.6 A g<sup>-1</sup>. The intimate binding of β-Ni(OH)<sub>2</sub> and graphene sheets afforded facile electron transport between individual nanoplates and the graphene sheets, which was a key to both the high Cs value and rate capability of the Ni(OH)<sub>2</sub>/graphene sheets composite. In another study, hierarchical flower-like Ni(OH)<sub>2</sub> decorated on graphene sheets presented a Cs value of 1735 F g<sup>-1</sup> at 1 mV s<sup>-1</sup> and remained 30% of its initial value with a scan rate incensement of 50 times, implying improved mass transportation, beneficial electron conduction within the nanoparticles and small equivalent series resistance [64]. Recently, a hierarchically porous graphene-Ni(OH)<sub>2</sub> hybrid hydrogel with both out-of-plane macropores and in-plane mesopores was fabricated by Chen et al. [65]. With the help of the hierarchical pores and good conductivity of the graphene sheets, the hybrid composite showed high Cs values in the current density range of 5–40 A g<sup>-1</sup> with good retention of Cs values, suggesting an enhanced rate capability. An alternative

approach worth noting is the work by Wang et al. [66]. Instead of decorating NiO or Ni(OH)<sub>2</sub> on graphene sheets, the authors wrapped β-Ni(OH)<sub>2</sub> hollow microspheres in reduced graphene oxides (rGO) to enhance the Cs values and rate capability of β-Ni(OH)<sub>2</sub>. The schematic illustration for the formation process of rGO/β-Ni(OH)<sub>2</sub> composite was shown in Fig. 3c, it can be seen that the β-Ni(OH)<sub>2</sub> hollow microspheres are tightly encapsulated by the flexible rGOs. The calculated Cs values of rGO/β-Ni(OH)<sub>2</sub> composite at different charging/discharging current density are presented in Fig. 3d and are 1552, 1382, 1254, 11924, 1143 F g<sup>-1</sup> at current densities of 2.67, 5.33, 10.67, 16, and 21.33 A g<sup>-1</sup> respectively. Even at 36.67 A g<sup>-1</sup>, the Cs value of the composite can be maintained at 1076 F g<sup>-1</sup>, indicating a good rate capability, which is quite crucial for the electrode of pseudocapacitors to achieve both high power and energy densities.

Ji et al. grew nanoporous Ni(OH)<sub>2</sub> thin film on the surface of ultrathin-graphite foam (UGF) via a hydrothermal reaction [67]. Fig. 3e depicts the Ni(OH)<sub>2</sub> film well adhered to the surface of UGF with a thickness of about 2 μm. The Cs value based on the total mass of the electrode was 166 F g<sup>-1</sup> at a current density of 0.5 A g<sup>-1</sup> (about  $(1.56 \pm 0.06) \times 10^3$  F g<sup>-1</sup> based on the mass of Ni(OH)<sub>2</sub> alone). When the current density was increased from 0.5 to 10 A g<sup>-1</sup>, the Cs value (based on the total mass of the electrode) decreased about 30% and then remained approximately constant for up to 111 A g<sup>-1</sup>, as shown in Fig. 3f. This rate performance highlights the advantages of the nanoporous Ni(OH)<sub>2</sub>/UGF composite. The highly conductive 3D UGF network ( $\sim 1.3 \times 10^5$  S m<sup>-1</sup> at 300 K) facilitates electron transport and the porous Ni(OH)<sub>2</sub> thin film structure shortens ion diffusion paths to achieve rapid migration of electrolyte ions.

As shown in Fig. 4a, Tang et al. deposited conformal Ni(OH)<sub>2</sub> onto the CVD grown dense carbon nanotube (CNT) bundles on nickel foam [68]. A remarkably high Cs value of 3300 F g<sup>-1</sup> at 1 mV s<sup>-1</sup>, and a lower capacity loss at a high charge/discharge current of 10 A g<sup>-1</sup> (about 33% of the Cs value at 2 A g<sup>-1</sup>) were achieved, as shown in Fig. 4b. The exceptional properties are believed attributable to a synergistic utilization of well-dispersed Ni(OH)<sub>2</sub> nano-flakes on the high surface area CNT/nickel foam current collector, high conductivity of CNT, and turbostratic disorder of α-Ni(OH)<sub>2</sub> structure. More recently, Dubal et al. decorated the outside surface of randomly MWCNTs with Ni(OH)<sub>2</sub> nanoparticles of less than 10 nm [69], as shown in Fig. 4c. Fig. 4d presents the cyclic voltammetry curves of the Ni(OH)<sub>2</sub>/MWCNTs composites with a mass loading of 30 mg cm<sup>-2</sup> at different scan rates. The

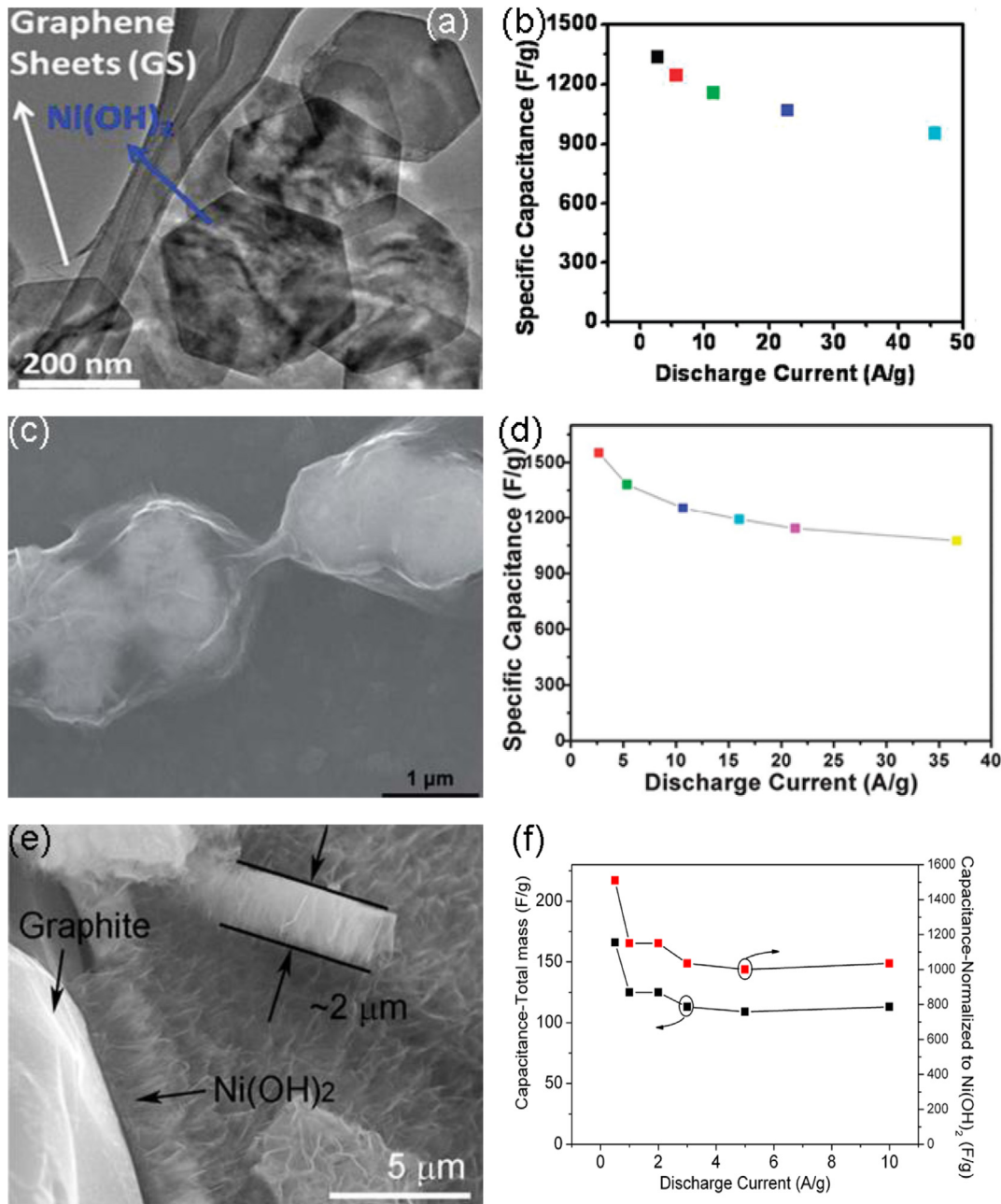


**Fig. 3.** TEM image (a) and Cs values at different discharging current densities (b); SEM image of  $\beta$ -Ni(OH)<sub>2</sub> coated on graphene sheets (c) and its Cs values at different discharging current densities (d); SEM image (e) and its Cs values at different discharging current densities (f) of nanoporous Ni(OH)<sub>2</sub> thin film adhered on the surface of ultrathin-graphite foam.

(a) & (b) reprinted with permission from Ref. [13]. Copyright 2010, American Chemical Society; (c) & (d) reprinted with permission from Ref. [66]. Copyright 2013, Royal Society of Chemistry; (e) & (f) reprinted with permission from Ref. [67]. Copyright 2013, American Chemical Society.

sponge-like Ni(OH)<sub>2</sub> and the uniform attachment to the MWCNTs led to a maximum Cs value of 1487 F g<sup>-1</sup> at a scan rate of 5 mV s<sup>-1</sup>. Furthermore, MWCNTs provide conducting pathway to facilitate a fast electrochemical kinetic process during high current density charge/discharge processes and the Cs value was reported to sustain at 998 F g<sup>-1</sup> at a high scan rate of 100 mV s<sup>-1</sup>.

In addition to graphene, its variants and CNTs, other carbon materials such as carbon nanoparticles and carbon fiber paper have also been researched to improve the electrochemical performance of NiO or Ni(OH)<sub>2</sub>. For example, monodispersed carbon nanoparticles encapsulated in hollow NiO showed a Cs value of 989 F g<sup>-1</sup> at a current density of 0.5 A g<sup>-1</sup> with good capacitive retention of

ca. 90.7% after 1000 charge/discharge cycles [70]. A composite electrode consisting of hybrid nanonet/nanoflower NiO deposited on carbon fiber paper scaffolds demonstrated an improved areal capacity (840 F g<sup>-1</sup>) while maintaining high rate capability and good cycling life [71].

### 3.2.2. Metal incorporated nickel oxide

Hybrid electrodes incorporating nickel oxide and selected metals have shown improved performances by enhancing the electronic conductivity of the electrode materials. Lu et al. fabricated NiO shells around the pellets of Ni nanoparticles by thermal annealing [21]. The composite possessed not only high Cs value of 910 F g<sup>-1</sup> but also

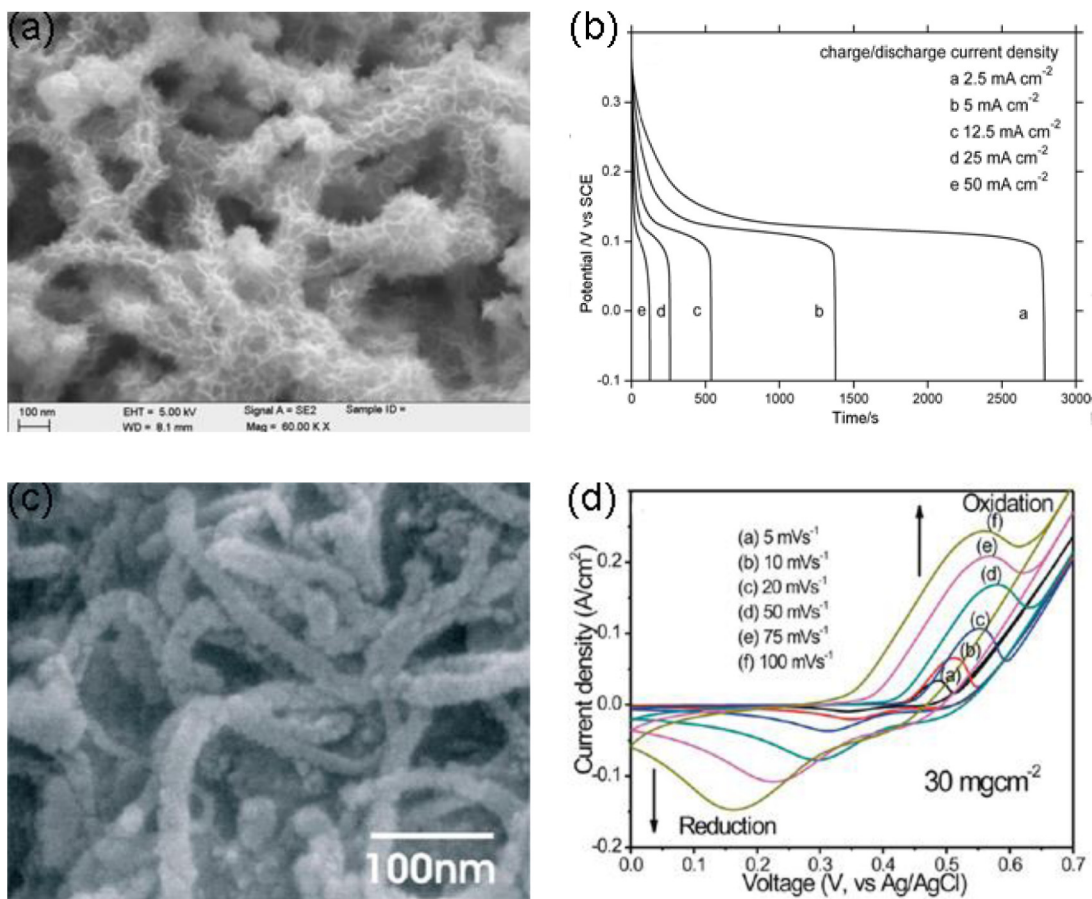


**Fig. 4.** SEM image (a) and its Cs values at different discharging current densities (b) of Ni(OH)<sub>2</sub> on dense CNT; SEM image (c) and cyclic voltammograms (d) of Ni(OH)<sub>2</sub> nanoparticles dotted on MWCNTs.

(a) & (b) reprinted with permission from Ref. [68]. Copyright 2012, Wiley-VCH Verlag GmbH & Co.; (c) & (d) reprinted with permission from Ref. [69]. Copyright 2013, American Chemical Society. Royal Society of Chemistry.

much higher power density of up to 28.6 A g<sup>-1</sup> (equivalent to 10 kW kg<sup>-1</sup> of power density). Hasan et al. synthesized coaxial NiO/Ni nanowire arrays through direct electrochemical deposition of Ni inside nanoporous alumina template and subsequent conversion of the outer shell into oxide by oxygen plasma annealing [72]. And almost at the same time, Kim et al. fabricated aligned Ni–NiO core–shell nanowire arrays on a glass substrate via electrochemical deposition using porous alumina oxide templates [73]. Although the core–shell arrays presented relatively low Cs values, they displayed good cycle performance and rate capability.

Besides Ni, Au and Ag are also chosen to be incorporated with nickel oxide to enhance the conductivity. Wu et al. prepared NiO/Ag composite film with the interconnecting reticular morphology made from NiO flakes with highly dispersed Ag nanoparticles of about 6 nm [74]. The NiO/Ag composite film exhibited Cs values of 330 F g<sup>-1</sup> at 2 A g<sup>-1</sup> and 281 F g<sup>-1</sup> at 40 A g<sup>-1</sup>, respectively, which were contributed to the improvement of the electric conductivity of the composite film by the highly dispersed Ag nanoparticles. More recently, hierarchical structures consisting of highly conductive Au nanoparticles decorated on NiO nanostructures were found to significantly improve electrical conductivity [75], resulting in a high Cs value of 619 F g<sup>-1</sup> at a high rate of 20 A g<sup>-1</sup>.

### 3.2.3. Transition metal oxides or hydroxides incorporated materials

Transition metal oxides or hydroxides incorporated NiO or Ni(OH)<sub>2</sub> composites have attracted considerable interest because of their enhanced characteristics over the single material. For

example, through calcination of mixed oxalate (Zn<sub>0.9</sub>Ni<sub>0.1</sub>(-C<sub>2</sub>O<sub>4</sub>)<sub>2</sub>·nH<sub>2</sub>O) precursors in air, Pang et al. synthesized ZnO–NiO composite with porous micropolyhedrons [76] and recorded an initial Cs value of 649 F g<sup>-1</sup> retained at 99.1% after 400 cycles at 5.8 A g<sup>-1</sup>. At a high current density of 58.0 A g<sup>-1</sup>, the Cs value still retained 395 F g<sup>-1</sup>. Favorable conductivity of ZnO and the novel interfaces between ZnO and NiO nanoparticles contribute to the high performance. Very recently, Xu et al. designed and fabricated hybrid NiO/Co<sub>3</sub>O<sub>4</sub> flower-like mesoporous architectures on a large scale by a facile, environmentally friendly, and low cost synthetic method [77]. The architectures showed a high Cs value of 1190 F g<sup>-1</sup> at a current density of 4 A g<sup>-1</sup>, a good rate capability at high current densities and a less than 1% loss of the maximum Cs value after 5000 cycles, which could be mainly attributed to their morphological characteristics of mesoporous and ultrathin nanosheets self-assembling into flower-like architectures as well as a rational composition of the two constituents. The rational composition not only fully utilizes individual constituents effectively, resulting from increasing the number of active sites, but also has a strong synergistic effect between NiO and Co<sub>3</sub>O<sub>4</sub> materials, thus shows high-performance in terms of both specific capacity and rate capability. Moreover, mesoporous nanosheet networks Co<sub>3</sub>O<sub>4</sub>/Ni(OH)<sub>2</sub> grown on conductive substrates were synthesized by heat treatment of Co(OH)<sub>2</sub>/Ni(OH)<sub>2</sub> precursor, and the composite achieved a high Cs value of 1144 F g<sup>-1</sup> at 5 mV s<sup>-1</sup> and long-term cyclability [78]. The authors attributed the improved electrochemical performances of Co<sub>3</sub>O<sub>4</sub>/Ni(OH)<sub>2</sub> composite to the factors such as binary redox

couples of  $\text{Ni}^{2+}/\text{Ni}^{3+}$  and  $\text{Co}^{2+}/\text{Co}^{3+}$ , nanosheet networks with porous structures, mesoporous structure within nanosheets, interconnections among nanosheets, and good electrical contact with the current collector. An important work on  $\text{Co}_3\text{O}_4/\text{NiO}$  composite electrode was done by Xia et al., who fabricated nanowire arrays on 3D macroporous nickel foam [79]. The electrodes exhibited a  $C_s$  value of  $853 \text{ F g}^{-1}$  at  $2 \text{ A g}^{-1}$  after 6000 cycles and an excellent cycling stability, especially, 85% of the capacity was maintained for the  $\text{Co}_3\text{O}_4/\text{NiO}$  core/shell nanowire arrays when the charge/discharge rate changed from 2 to  $40 \text{ A g}^{-1}$ , which could be owing to the unique porous core/shell nanowire array architecture, and a rational combination of two electrochemically active materials. In order to improve the area capacity, an alternative method was to coat  $\text{Ni(OH)}_2$  nanolayers on the surface of aligned and cross-linked  $\text{CoO}$  [80]. The  $C_s$  value of this composite was up to about  $2374 \text{ F g}^{-1}$  at  $1.03 \text{ A g}^{-1}$ , and the authors ascribed it to a much increased surface area offered by its hierarchically porous structure, as well as a possible synergistic effect between the two materials. Moreover, Jiang et al. fabricated a triple composite of 3 components  $\text{Ni(OH)}_2/\text{CoO/rGO}$  [81]. The synergistic effects of  $\text{Ni(OH)}_2$  and  $\text{CoO}$  and a good electrical conductivity provided by rGO endued the composite of improved supercapacitor properties such as a  $C_s$  value of  $1317 \text{ F g}^{-1}$  at a current density of  $2 \text{ A g}^{-1}$  and good cyclability. Another example of triple composites was mesoporous Ni–Co oxides nanowire arrays on ordered  $\text{TiO}_2$  nanotubes synthesized by Yang et al. [82]. The composite had both superior conductivity and aligned structure of the Ni–Co oxides nanowires and the  $\text{TiO}_2$  nanotubes, which could improve electron/ion transport and enhance the kinetics of the redox reactions. The composite electrode presented a high  $C_s$  value of  $2353 \text{ F g}^{-1}$  at a current density of  $2.5 \text{ A g}^{-1}$  with excellent cycling ability, and retained 95% of the maximum capacity after 3000 cycles. At a high current density of  $50 \text{ A g}^{-1}$ , the electrode exhibited a  $C_s$  value of up to  $2173 \text{ F g}^{-1}$ , which showed a good rate capability. Triple composite of nickel cobalt layered double hydroxides on conducting  $\text{Zn}_2\text{SnO}_4$  nanowires was also reported [83]. This novel material demonstrated outstanding electrochemical performance with a high  $C_s$  value of  $1805 \text{ F g}^{-1}$  at  $0.5 \text{ A g}^{-1}$ , and an excellent rate performance of  $1275 \text{ F g}^{-1}$  could be achieved at  $100 \text{ A g}^{-1}$ .

#### 3.2.4. Other $\text{NiO}$ or $\text{Ni(OH)}_2$ composites

Except the above composites, some less common compounds have also been adopted by researchers to improve the supercapacitor performance of nickel oxide or hydroxide. For instance, Yuan et al. prepared a porous net-like  $\beta\text{-Ni(OH)}_2/\alpha\text{-NiOOH}$  composite film [84]. The as-prepared porous composite film showed a highly porous structure built up by many interconnected nanoflakes with a thickness of about 20 nm. And the film exhibited a  $C_s$  value of  $1420 \text{ F g}^{-1}$  at  $2 \text{ A g}^{-1}$  and  $1098 \text{ F g}^{-1}$  at  $40 \text{ A g}^{-1}$ , respectively. Another example is sponge-like porous  $\text{Ni(OH)}_2\text{-NiF}_2$  composite film synthesized by Jin et al. through the anodization of nickel in a  $\text{NH}_4\text{F}$  and  $\text{H}_3\text{PO}_4$  containing electrolyte [85]. The film exhibited not only a high  $C_s$  value of  $2090 \text{ F g}^{-1}$  at  $10 \text{ mV s}^{-1}$  but also a superior rate capability and a good cyclability (capacity retained more than  $1200 \text{ F g}^{-1}$  at  $100 \text{ A g}^{-1}$  after 2000 cycles), which was owned to the good conductivity and the highly porous architecture. Recently, Liang et al. developed a mesoporous  $\text{LaNiO}_3/\text{NiO}$  electrode for thin film supercapacitor from the sol–gel precursor using polyethylene glycol 1000 as a template [86]. The authors proved that  $\text{LaNiO}_3$  could enhance the electrical conductivity and stability of the electrodes, and the porous structure could provide full accessibility of the electrolyte, which was helpful in improving the stable performance of the electrochemical behaviors.

In the above composites, the presence of additive agent not only improves the electrical conductivity of  $\text{NiO}$  or  $\text{Ni(OH)}_2$  but also increases its active surface area and improves its  $C_s$  value. These additive agents can promote a three-dimensional porous conducting network to effectively assist electron transfer and ion transport within  $\text{NiO}$  or  $\text{Ni(OH)}_2$  materials, thereby improving their rate capability and cycle performance.

### 3.3. Developing new nickel based materials

#### 3.3.1. $\text{NiCo}_2\text{O}_4$

In contrast to composites where distinctive components are mixed or constructed to achieve optimized performances, ternary compounds attracted extensive investigation in recent years have elemental or phase constituents which can maintain intrinsic thermodynamic stability while affording elemental or phase tunability for superior electrochemical properties. An example is the ternary nickel cobaltite ( $\text{NiCo}_2\text{O}_4$ ) which has electrical conductivity of 2–3 magnitude higher than that of conventional transition metal oxides and higher electrochemical activity than the binary oxides of  $\text{NiO}$  and  $\text{Co}_3\text{O}_4$ . Lu et al. fabricated a  $\text{NiCo}_2\text{O}_4$  electrode with a highly ordered mesoporous structure and nanocrystalline walls using a hard-template method [22]. By simultaneously tailoring electrode conductivity, pore size dispersion, and crystallinity, the material showed a most promising supercapacitor performance of  $10 \text{ kW kg}^{-1}$  power density at  $28 \text{ Wh kg}^{-1}$ , and more than 95% capacity was retained after 2500 cycles at a high power density of  $10 \text{ kW kg}^{-1}$ . More importantly, the active mass loading on the electrode was larger than  $10 \text{ mg cm}^{-2}$ , which is desired for a commercial device.

Through co-electrodeposition of a bimetallic (Ni, Co) hydroxide precursor on a Ni foam support and subsequent thermal transformation, Lou's group synthesized spinel mesoporous  $\text{NiCo}_2\text{O}_4$  nanosheets [87]. The as-prepared ultrathin  $\text{NiCo}_2\text{O}_4$  nanosheets exhibited folding silk-like morphology with a nanosheet thickness of only 2–4 nm, and there were numerous inter-particle mesopores with a size ranged from 2 to 5 nm in these ultrathin nanosheets, as shown in Fig. 5a and b. The ultrathin mesoporous  $\text{NiCo}_2\text{O}_4$  nanosheets electrode demonstrated  $C_s$  values of 2010, 1859, 1694, 1596 and  $1450 \text{ F g}^{-1}$  at current densities of 2, 4, 8, 12 and  $20 \text{ A g}^{-1}$ , respectively. Following the above work, this group deposited single-crystalline  $\text{NiCo}_2\text{O}_4$  nanowire arrays on conductive substrates such as Ni foam and Ti foil through a simple solution method and a post-annealing treatment [88]. They directly utilized the Ni foam supported  $\text{NiCo}_2\text{O}_4$  nanowire arrays as binder-free electrodes for supercapacitors. Remarkably, the  $\text{NiCo}_2\text{O}_4\text{-Ni}$  electrode exhibits greatly improved electrochemical performance with very high capacity normalized with area or mass and greatly improved cycling stability compared to other array electrodes and free-standing porous  $\text{NiCo}_2\text{O}_4$  nanowires. Recently, the same group fabricated interconnected  $\text{NiCo}_2\text{O}_4$  mesoporous nanosheets on various conductive substrates through a facile solution method combined with a simple post heat treatment [89], and proved that the  $\text{NiCo}_2\text{O}_4$  nanosheets-Ni foam electrode presented remarkable electrochemical performance with ultrahigh capacity and good cycling stability.

Fig. 5c shows a 1D  $\text{NiCo}_2\text{O}_4$  nanotubes architecture with a porous structure and hollow interiors prepared by a single-spinneret electrospinning technique followed by calcination in air [90]. This unique structure exhibited a high  $C_s$  value of  $1647 \text{ F g}^{-1}$  at  $1 \text{ A g}^{-1}$ , good rate capability (77.3% capacity retention at  $25 \text{ A g}^{-1}$ ), as shown in Fig. 5d, and outstanding cycling stability due to a relatively large specific surface area.

While the specific surface area, together with the feature dimension and porosity, plays essential roles in enhancing

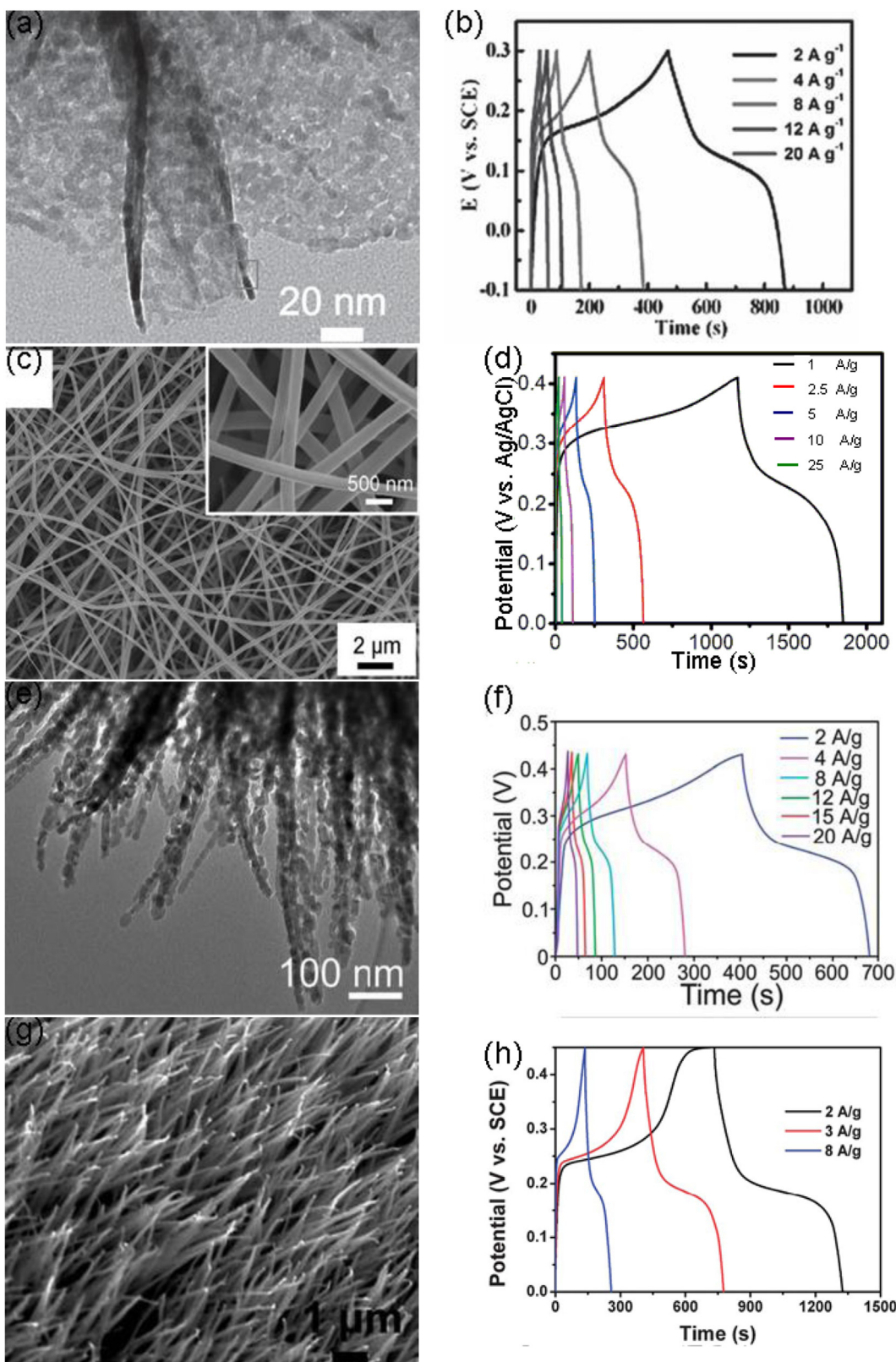


**Fig. 5.** TEM image (a) and discharging curves at different current densities (b) of ultrathin  $\text{NiCo}_2\text{O}_4$  nanosheets; SEM image (c) and discharging curves at different current densities (d) of ultrathin  $\text{NiCo}_2\text{O}_4$  nanotubes; SEM image (e) and discharging curves (f) of chain-like  $\text{NiCo}_2\text{O}_4$  nanowires; SEM image (g) and discharging curves at different current densities (h) of aligned  $\text{NiCo}_2\text{O}_4$  nanowire arrays on Ni foam.  
 (a) & (b) reprinted with permission from Ref. [87]. Copyright 2012, Wiley-VCH Verlag GmbH & Co.; (c) & (d) reprinted with permission from Ref. [90]. Copyright 2013, Wiley-VCH Verlag GmbH & Co.; (e) & (f) reprinted with permission from Ref. [91]. Copyright 2013, Royal Society of Chemistry; (g) & (h) reprinted with permission from Ref. [95]. Copyright 2013, Royal Society of Chemistry.

supercapacitance, the electrochemical activity of individual crystal planes may vary. Zou et al. verified the contribution of atomic planes of  $\text{NiCo}_2\text{O}_4$  to the high  $C_s$  values [91]. They prepared 3D  $\text{NiCo}_2\text{O}_4$  micro-sphere constructed from radial chain-like  $\text{NiCo}_2\text{O}_4$  nanowires with exposed different crystal planes, as depicted in Fig. 5e, and this material exhibited high electrochemical performances with a  $C_s$  value of  $1284 \text{ F g}^{-1}$  at  $2 \text{ A g}^{-1}$  (see Fig. 5f), good rate capability and good cycling stability, respectively. Experimental results provided by different groups also confirmed that nickel cobaltite nanowire was an effective materials for electrochemical pseudocapacitors and that the coexistence of nickel and cobalt ions, mesoporous characteristics, and nanocrystal structure were important for high electrochemical performance [92,93].

Beyond what has been stated, nickel cobaltite aerogels, a low-cost mesoporous material with highly specific surface area, porosity, electronic conductivity, as well as electrochemical activity and multiple oxidation states/structures, was prepared by Wei et al. through an epoxide-driven sol/gel process [94]. When calcined at  $200^\circ\text{C}$ , the obtained product could achieve an extremely  $C_s$  value of  $1400 \text{ F g}^{-1}$  after a 650 cycle activation and the retained  $C_s$  value after a 2000-cycle test is about 91% of the maximum value. Chen et al. synthesized porous  $\text{NiCo}_2\text{O}_4$  flowerlike nanostructure via a simple hydrothermal and subsequent annealing process [95]. The obtained  $\text{NiCo}_2\text{O}_4$  delivered an enhanced specific capacitance of  $658 \text{ F g}^{-1}$  at  $1 \text{ A g}^{-1}$ , and 77% specific capacitance retention for a 50-time scan rate rise was achieved. The  $\text{NiCo}_2\text{O}_4$  sample demonstrated ultra long cycling lifespan, no observable degradation was observed for the total cycle numbers as high as 10,000. The authors pointed out that the high conductivity and the unique porous 3D flowerlike structure should account for the good capacitive performances of the as-prepared  $\text{NiCo}_2\text{O}_4$  material. Through a rapid and template-free microwave-assisted heating reflux followed by pyrolysis of as-prepared precursors, Lei et al. fabricated three-dimensional hierarchical flower-shaped nickel cobaltite microspheres with improved electrical conductivity and effective porous structure [96]. The as-fabricated  $\text{NiCo}_2\text{O}_4$  exhibited high specific capacitance of  $1006 \text{ F g}^{-1}$  at  $1 \text{ A g}^{-1}$ , and excellent electrochemical stability with 93.2% retention after 1000 continuous charge/discharge cycles at a high current density of  $8 \text{ A g}^{-1}$ . Zhang et al. suggested that a suitable capping agent was very helpful for controlling the morphology of the  $\text{NiCo}_2\text{O}_4$  in a hydrothermal process [97]. The  $\text{NiCo}_2\text{O}_4$  synthesized without the presence of polyvinylpyrrolidone presented a three dimensional hierarchical flower-like architecture, in contrast, the  $\text{NiCo}_2\text{O}_4$  synthesized in the presence of polyvinylpyrrolidone exhibited an intimately interconnected hierarchical mesoporous structure with a uniform distribution. The specific capacitance of 3D flower-like  $\text{NiCo}_2\text{O}_4$  was about  $797.3 \text{ F g}^{-1}$ , while that of hierarchical mesoporous  $\text{NiCo}_2\text{O}_4$  is about  $1619.1 \text{ F g}^{-1}$  at a current density of  $2.0 \text{ A g}^{-1}$  in each case. Compared with the 3D flower-like  $\text{NiCo}_2\text{O}_4$ , hierarchical mesoporous structured  $\text{NiCo}_2\text{O}_4$  also presented good cycling stability. Lu et al. fabricated hierarchical  $\text{NiCo}_2\text{O}_4$  nanosheets@hollowmicrorod arrays by a simple and environmentally friendly template-assisted electrodeposition followed by thermal annealing [98]. The  $\text{NiCo}_2\text{O}_4$  exhibited a high specific capacitance of  $678 \text{ F g}^{-1}$  at  $6 \text{ A g}^{-1}$  and outstanding cycle stability. The high capacitive performance could be attributed to the large specific surface area of the  $\text{NiCo}_2\text{O}_4$ , fast ion diffusion, and perfect charge transmission in the hierarchical materials.

In order to fabricate flexible all-solid-state supercapacitors, Wang et al. synthesized  $\text{NiCo}_2\text{O}_4$  nanowire arrays supported on Ni foams as supercapacitor electrode [99]. As presented in Fig. 5g, there were numerous nanowires grown vertically on the whole Ni foam to form highly aligned nanowire arrays, and the lengths and diameters of the nanowires were about 3 mm and 80–200 nm,

respectively. This material exhibited wonderful pseudocapacitor behaviors with  $C_s$  values of 2681, 2524 and  $2305 \text{ F g}^{-1}$  at current densities of 2, 3 and  $8 \text{ A g}^{-1}$ , respectively, as shown in Fig. 5h. By assembling two pieces of the as-grown  $\text{NiCo}_2\text{O}_4$  nanowire electrodes, a simple all-solid-state supercapacitor was fabricated. The device showed an improved rate capability, and the electrochemical performances of the device do not significantly change in both the twisted and bent states.

Different from the stable mixed oxide  $\text{NiCo}_2\text{O}_4$ , Xiao et al. synthesized NaCl-type  $\text{Co}_x\text{Ni}_{1-x}\text{O}$  ( $0 < x < 1$ ) nanorods on rGO sheets and screened for asymmetric electrochemical capacitors through a bio-inspired approach [100]. They demonstrated that a key was the crystallization process from amorphous precursors in a disordered and hydrated state being able to take compositions arbitrarily. For example, the as-prepared  $\text{Co}_{0.45}\text{Ni}_{0.55}\text{O}/\text{rGO}$  nanocomposite electrode exhibited a  $C_s$  value of  $909 \text{ F g}^{-1}$  at  $1 \text{ A g}^{-1}$ , and with a surprising increase of the specific capacity in the initial 100 cycles before flattened out.

Although great success has been achieved with  $\text{NiCo}_2\text{O}_4$  for supercapacitor applications, significant improvements are still possible by further enhancing the specific surface area and electric conductivity of the electrode together with a better utilization of  $\text{NiCo}_2\text{O}_4$ . In order to further improve the  $C_s$  value and cycling stability of  $\text{NiCo}_2\text{O}_4$ , Wang et al. synthesized fine  $\text{NiCo}_2\text{O}_4$  on functionalized single wall carbon nanotube bundles by controlled hydrolysis reaction in organic/water mixed solvent system [101]. Contributed to the reduced resistance of the nanocomposite, this novel material not only exhibited a high  $C_s$  value of  $1642 \text{ F g}^{-1}$  but also showed good rate capability as well as good long time cycling stability at high mass loading. Another valuable work was done by Chien et al. [102]. With a two-step wet chemistry process, they deposited nickel cobaltite with a thin nanostructure of 3–5 nm nanocrystals into mesoporous carbon to improve high surface areas and electric conductivities. By using highly conductive mesoporous carbon aerogels as the host matrix and the successful creation of an ultrathin  $\text{NiCo}_2\text{O}_4$  nanostructure on the backbone of the matrix, the  $\text{NiCo}_2\text{O}_4$  was fully utilized. Thereby, the nickel cobaltite/carbon aerogel composite showed high  $C_s$  value of around  $1700 \text{ F g}^{-1}$  at a scan rate of  $25 \text{ mV s}^{-1}$ , high rate capability manifested by maintaining  $C_s$  values above  $800 \text{ F g}^{-1}$  at a high scan rate of  $500 \text{ mV s}^{-1}$ , and outstanding cycling stability demonstrated by a negligible 2.4% decay in  $C_s$  values after 2000 cycles. Wang et al. grew nickel cobaltite nanowires and nanosheets on carbon cloth through adjusting the experimental parameters [103]. They discovered that the  $\text{NiCo}_2\text{O}_4$  nanowires/carbon cloth showed higher specific capacity and better cycling performance than that of the  $\text{NiCo}_2\text{O}_4$  nanosheets/carbon cloth, which was related to the surface area and pore structure of  $\text{NiCo}_2\text{O}_4$  nanocrystals. Recently, two-dimensional ultrathin mesoporous  $\text{NiCo}_2\text{O}_4$  nanosheets on carbon fiber paper were synthesized by Deng et al. through a solvothermal method combined with a post thermal treatment [104]. The authors pointed out that the well interconnected ultrathin  $\text{NiCo}_2\text{O}_4$  nanosheets directly grown on the carbon nanofibers could allow for easy diffusion of the electrolyte, shorten the transport path of ion and electron and accommodate the strain during cycling. The materials exhibited high specific capacitance of  $999 \text{ F g}^{-1}$  at a current density of  $20 \text{ A g}^{-1}$ , and the capacitance loss was 15.6% after 3000 cycles at a current density of  $10 \text{ A g}^{-1}$ , displaying good cycle ability and high rate capability. Padmanathan and Selladurai demonstrated that the surface morphology of  $\text{NiCo}_2\text{O}_4$  was driven by varying the precursors [105]. They fabricated  $\text{NiCo}_2\text{O}_4$  nanowall-networks and porous nanoflake microstructures grown on carbon fiber cloth by using the nitrate and chloride precursors respectively. As an advantage of their unique structural features, they showed different capacitive performance. The as-grown  $\text{NiCo}_2\text{O}_4$  nanowall-

network structure delivered a maximum capacitance of  $1225 \text{ F g}^{-1}$  at a current density of  $5 \text{ A g}^{-1}$  and excellent durability. However, a limited specific capacitance of  $844 \text{ F g}^{-1}$  was achieved at a current density of  $1 \text{ A g}^{-1}$  for  $\text{NiCo}_2\text{O}_4$  nanoflakes. The variation in capacitive performance such as specific capacitance, rate capability and cyclic stability was mainly due to structural discrepancies. And the authors concluded that precursors with different anions also greatly influence the growth kinetics of metal oxide nanostructures. Through a facile electrochemical deposition method followed by subsequent annealing in air, Liu et al. have built a 3D vertically aligned carbon nanotube/ $\text{NiCo}_2\text{O}_4$  core/shell nano-architecture [106]. In a  $6 \text{ mol L}^{-1}$  KOH electrolyte, the vertically aligned core/shell structures exhibited a specific capacitance of  $695 \text{ F g}^{-1}$  at a current density of  $1 \text{ A g}^{-1}$ , and the specific capacitance still remained nearly 82% of the initial capacitance value at a high current density of  $20 \text{ A g}^{-1}$ . The authors contributed it to the unique 3D vertically aligned core/shell structures, which could support fast ion/electron transport in the electrode and at the electrolyte/electrode interface.

In addition to carbon materials, metal oxides were also adopted to improve the electrochemical performance of  $\text{NiCo}_2\text{O}_4$ . Yang et al. fabricated hierarchical  $\text{NiCo}_2\text{O}_4@\text{NiO}$  core–shell nanowire hetero-nanostructure anchored on a carbon cloth [107]. Impressively, a high specific capacitance of  $1792 \text{ F g}^{-1}$  at about  $4.2 \text{ A g}^{-1}$  was achieved, along with excellent rate capability and cycle performance (with the capacity retention of 87.5% after 5000 cycling). The outstanding electrochemical performances could be attributed to its superstructure with significantly enhanced active-surface area, favorable morphological stability and convenient ion transport paths. Xu et al. fabricated hierarchical mesoporous  $\text{NiCo}_2\text{O}_4@\text{MnO}_2$  core–shell nanowire arrays on nickel foam via a facile hydrothermal and electrodeposition process [108]. The materials showed high specific capacitance of  $1870 \text{ F g}^{-1}$  at a current density of about  $1.67 \text{ A g}^{-1}$ . And the overall specific capacitance retention for the  $\text{NiCo}_2\text{O}_4@\text{MnO}_2$  electrode was about 113.6% after 8000 cycles at a scan rate of  $50 \text{ mV s}^{-1}$ .

### 3.3.2. NiS and other nickel based materials

After the first report of applying NiS as a supercapacitor electrode and proposing an electrochemical reaction mechanism by Hou et al. [109], Zhu et al. investigated the improved electrochemical performance of nickel sulfide by designing and fabricating hierarchical hollow structures [110]. Recently, by using diethanolamine as the coordination agent and solvent, Yang et al. synthesized hierarchical flower-like  $\beta$ -NiS architecture via a solvothermal method [111]. The authors investigated the influence of experimental parameters such as reacting time and the amount of diethanolamine on the morphologies of the final products, and demonstrated that NiS with the flower-like morphology had good electrochemical performance with a  $C_s$  value of  $710 \text{ F g}^{-1}$  at a current density of  $2 \text{ A g}^{-1}$ , a coulombic efficiency of about 99% and good rate capability. In addition, the supercapacitor performance of  $\text{Ni}_3\text{S}_2$  was also investigated. Chou et al. deposited flaky  $\text{Ni}_3\text{S}_2$  nanostructures on a Ni foam substrate using a facile potentiodynamic deposition approach and investigated this electroactive material for high-performance supercapacitor [112]. The as-prepared  $\text{Ni}_3\text{S}_2$  nanostructure was assembled from intercrossing nanoflakes, which facilitating the electrolyte penetration. Thereby, the flaky  $\text{Ni}_3\text{S}_2$  nanostructure showed a  $C_s$  value of  $717 \text{ F g}^{-1}$  at  $2 \text{ A g}^{-1}$ , and a remarkable rate capability, in which a promising  $C_s$  value of  $411 \text{ F g}^{-1}$  could still be delivered at  $32 \text{ A g}^{-1}$ . Moreover, the flaky  $\text{Ni}_3\text{S}_2$  nanostructure demonstrated an impressive cycling performance.

Another nickel based material used as supercapacitor electrode is hydroxide nitrate nanoflake. Liu et al. utilized an ultrathin nickel

hydroxide nitrate nanoflake – ZnO nanowire hybrid array as high rate pseudocapacitive energy storage [113]. In their report, the hybrid array showed a high  $C_s$  value of  $1310 \text{ F g}^{-1}$  at a charge/discharge current density of  $15.7 \text{ A g}^{-1}$ . In order to further improve its pseudocapacitive performance, Kong et al. synthesized flower-like  $\text{Ni}_3(\text{NO}_3)_2(\text{OH})_4$  and systematically studied the experimental factors such as the concentrations of reactant and temperature on the microstructure and specific capacity of the prepared products [114]. The experimental results indicated that the flower-like structure formed from petal-like nanoflakes with a thickness of approximately 50 nm had a profound impact on electrode performance at high discharge capacity. A maximum  $C_s$  value of  $2212 \text{ F g}^{-1}$  could be achieved at the current density of  $5 \text{ mA}$  and be retained about 54% at  $50 \text{ mA}$  (the electrode contained about 4 mg of electroactive material and had a geometric surface area of about  $1 \text{ cm}^2$ ). After 1000 continuous cycles at  $5 \text{ mA}$ , the  $C_s$  value reduced to  $1512 \text{ F g}^{-1}$ , remained 68% of that of the early cycle. These results support its potential application as a viable electrode material for electrochemical capacitors.

In high-concentrated basic solution at room temperature,  $\text{Ni}_{0.25}\text{Co}_{0.75}(\text{OH})_2$  hierarchical nanowire@nanoplatelets arrays were prepared by an *in-situ* conversion from the precursor of  $\text{Ni}_{0.5}\text{C}_{0.5}(\text{OH})_2\text{CO}_3$  nanowire@nanoplatelets arrays grown on Ni foam substrate by a hydrothermal method [115]. Compared with the precursor, the  $\text{Ni}_{0.25}\text{Co}_{0.75}(\text{OH})_2$  hierarchical nanowire@nanoplatelets arrays demonstrated superior electrochemical performance including high  $C_s$  value of  $928 \text{ F g}^{-1}$  at  $0.58 \text{ A g}^{-1}$ , 81% retention at a current density of  $5.8 \text{ A g}^{-1}$  and good cycling stability.

## 4. $De$ and $Dp$ of nickel based materials

Except  $C_s$  value, rate capability and cycle life, the key parameters of supercapacitors and their potential for practical applications also include energy density and power density. The power density and energy density ranges of some recent reported nickel based materials are listed in Tables 2–4.

From Table 2, it can be seen that a hierarchically porous NiO film with a structure of triangular prisms and randomly porous nanoflakes delivers a high energy density of about  $30 \text{ Wh kg}^{-1}$  at a high power density of  $5.5 \text{ kW kg}^{-1}$  [45]. As for porous NiO microflowers materials synthesized from a coordination microflower precursor [50], the  $De$  value is  $45.6 \text{ Wh kg}^{-1}$  at  $Dp 139.3 \text{ W kg}^{-1}$ , especially, when the  $Dp$  value is  $1405.5 \text{ W kg}^{-1}$ , the  $De$  remains at  $22.1 \text{ Wh kg}^{-1}$ , which makes it to be a promising candidate of supercapacitor electrode material. The highest  $De$  and  $Dp$  values of NiO materials were reported in Liang's studies [47]. Through a two-step electrochemical process, they prepared a 3D nanoporous NiO film with the maximum  $Dp$  value of  $89 \text{ Wh kg}^{-1}$  and highest  $De$  value of  $16.5 \text{ kW kg}^{-1}$ . Importantly, the power density met the power requirement of the Partnership for a New Generation of Vehicles (PNGV). In addition, when the  $Dp$  values increased from  $0.3 \text{ Wh kg}^{-1}$  to  $16.5 \text{ kW kg}^{-1}$ , the  $De$  values only decreased from 89 to  $63 \text{ Wh kg}^{-1}$ , which showed potential application in electrochemical capacitors.

**Table 2**  
The  $De$  and  $Dp$  ranges of some reported NiO materials.

Materials	Electrolyte	$De$ range ( $\text{Wh kg}^{-1}$ )	$Dp$ range ( $\text{kW kg}^{-1}$ )	Reference
hierarchically porous NiO	$1 \text{ mol L}^{-1}$ KOH	30–35	5.5–0.4	[45]
3D nanoporous NiO	$1 \text{ mol L}^{-1}$ KOH	63–89	16.5–0.3	[47]
NiO microflowers	$\sim 0.5 \text{ mol L}^{-1}$ KOH	22.1–45.6	1.41–0.14	[50]
NiO nano sheets	$6 \text{ mol L}^{-1}$ KOH	24–35	4.8–1.9	[57]

**Table 3**

The  $De$  and  $Dp$  ranges of some reported NiO composites.

Composites	Electrolyte	$De$ range (Wh kg <sup>-1</sup> )	$Dp$ range (kW kg <sup>-1</sup> )	Reference
NiO/Graphene	1 mol L <sup>-1</sup> KOH	37–54	10–1.6	[13]
NiO/Ni	1 mol L <sup>-1</sup> KOH	26–60	10–0.4	[21]
NiO/ZnO	1 mol L <sup>-1</sup> KOH	12–20	18–1.8	[76]

The relationships between  $De$  and  $Dp$  of some of recent reported nickel based composites were listed in Table 3. Pang et al. explored the application of porous ZnO–NiO composite micropolyhedrons through calcination of  $Zn_{0.9}Ni_{0.1}(C_2O_4)_2 \cdot nH_2O$  at different temperatures as electrochemical capacitors [76]. When calcined at 400 °C for 10 min and applied in a electrolyte of 3.0 mol L<sup>-1</sup> KOH, the specific energy densities of the ZnO–NiO composite decreased from 19.9 to 12.1 Wh kg<sup>-1</sup>, while the specific power increased from 1581 to 15,709 W kg<sup>-1</sup> as the charge/discharge current increased from 5.8 to 58.0 A g<sup>-1</sup>. Single-crystalline Ni(OH)<sub>2</sub> hexagonal nanoplates grown on graphene sheets presented a high  $De$  of about 37 Wh kg<sup>-1</sup> at a high  $Dp$  value of about 10 kW kg<sup>-1</sup>, which was better than that of Ni(OH)<sub>2</sub> nanoplates simply mixed with graphene sheets and Ni(OH)<sub>2</sub> nanoparticles grown on graphene oxides [13]. Lu et al. have pointed out that supercapacitor electrodes prepared from monolithic NiO/Ni nanocomposites could have both high energy and power densities [21]. In their studies, a  $De$  value of 62 Wh kg<sup>-1</sup> (equivalent to 905 F g<sup>-1</sup> for the Cs) was observed at a  $Dp$  value of 0.4 kW kg<sup>-1</sup>. As the charge/discharge rate was increased to 28.6 A g<sup>-1</sup>, a high  $Dp$  value of 10 kW kg<sup>-1</sup> was achieved, and the corresponding  $De$  value dropped to 26 Wh kg<sup>-1</sup> (equivalent to 380 F g<sup>-1</sup> for the Cs value). However, it is still one of best reported performances.

The  $De$  and  $Dp$  range of some reported NiCo<sub>2</sub>O<sub>4</sub> materials are listed in Table 4. For hierarchical porous NiCo<sub>2</sub>O<sub>4</sub> nanowires, the  $De$  was be estimated to be 22.6 Wh kg<sup>-1</sup> at a  $Dp$  value of 219 W kg<sup>-1</sup> [93], and the  $De$  was still as high as 13.9 Wh kg<sup>-1</sup> even at a high  $Dp$  value of 6854.8 W kg<sup>-1</sup>. These results mean that the hierarchical porous NiCo<sub>2</sub>O<sub>4</sub> nanowires will be a promising pseudocapacitor electrode material for high-rate charge/discharge operations. Porous NiCo<sub>2</sub>O<sub>4</sub> nanotubes, synthesized by Li et al., could possess a  $De$  value of 38.5 Wh kg<sup>-1</sup> at a  $Dp$  value of 205 W kg<sup>-1</sup> [91], which was about 1.6 and 2.0 times those of the NiCo<sub>2</sub>O<sub>4</sub> nanofibers and NiCo<sub>2</sub>O<sub>4</sub> nanobelts, respectively. At a  $Dp$  value of 5 kW kg<sup>-1</sup>, the sample of NiCo<sub>2</sub>O<sub>4</sub> nanowire, prepared from equimolar nickel acetate and cobalt acetate, could still deliver an  $De$  value of 19.72 Wh kg<sup>-1</sup> [92], which is about three to four times those of carbon-based supercapacitors in KOH electrolyte.

To clearly compare the power and energy capabilities of some nickel based materials, their  $Dp$  and  $De$  ranges are delineated in Fig. 6. It can be seen that the  $De$  values of most recently reported nickel based materials are improved, and their  $Dp$  values are large than batteries. The maximum  $Dp$  value was 89 Wh kg<sup>-1</sup> with corresponding  $De$  value at 16.5 kW kg<sup>-1</sup>, which was obtained in a three-dimensional nanoporous NiO film [47]. The reported  $Dp$  and  $De$  ranges of nickel based composites are usually large than NiCo<sub>2</sub>O<sub>4</sub>

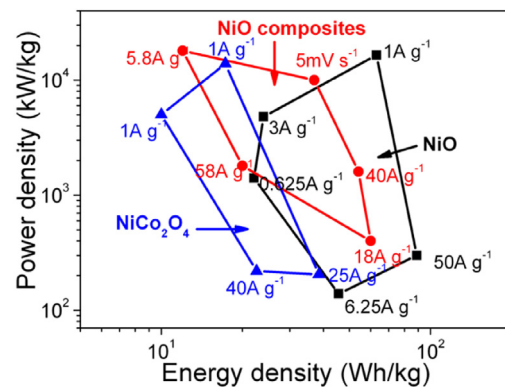


Fig. 6. The  $Dp$  and  $De$  ranges of some nickel based materials. The corresponding current densities are presented on this Ragone plot.

materials, the improved conductivity of nickel based composites may contribute to this result. Although there is a notable progress in improving the  $De$  and  $Dp$  values of nickel based materials, the  $Dp$  values cannot reach the level of most traditional capacitors, and the  $De$  values are still less than 100 Wh kg<sup>-1</sup>.

It should be pointed out that all the  $De$  and  $Dp$  were measured at a narrow potential window of about 0.5 V against the reference electrode. If these materials are coupled with a suitable counter-electrode material, a large potential window may be utilized.

## 5. Summary and outlook

In summary, we have evaluated recent advances in nickel based materials for high performance pseudocapacitor electrodes. The Cs values of nickel based materials are determined by the interaction of morphology, particle size, specific surface area and pore properties. By forming composites, nickel based materials can overcome the poor conductivity and improve the rate capability and cycling stability. Due to improved conductivities and synergic effects, the pseudocapacitive behaviors of composite materials can be greatly enhanced and they usually demonstrate high Cs values, high rate capabilities and good charge/discharge cycling stabilities. For the purpose of practical applications, we have also summarized and compared the  $De$  and  $Dp$  values of some recently reported NiO, nickel based composites and NiCo<sub>2</sub>O<sub>4</sub>. Although the  $De$  and  $Dp$  values of nickel based materials are improved by tailoring their morphology and structure or forming composites, the reported  $De$  and  $Dp$  values are still short of what are desired for practical applications.

It is our opinion that the trends of nickel based materials for high-performance pseudocapacitors may include the following:

- (1) Further increasing the Cs value by controlling the morphology, particle size, and surface area and pore properties. It is worth to point out that although some reported nickel materials can achieve high Cs values and rate capability due to increased electrical conductivity, these materials may not necessarily be ideal electrode materials in a real application. Because when it is used to construct a thicker electrode layer, the electrochemical utilization of the material and ionic transport throughout the internal volume of the thicker electrode layer will be limited.
- (2) Improving the conductivity through forming composite materials. Composites can not only overcome the drawbacks of individual components but also embody the advantages of all constituents. In addition, a synergistic effect often times

**Table 4**

The  $De$  and  $Dp$  ranges of some reported NiCo<sub>2</sub>O<sub>4</sub> materials.

Materials	Electrolyte	$De$ range (Wh kg <sup>-1</sup> )	$Dp$ range (kW kg <sup>-1</sup> )	Reference
NiCo <sub>2</sub> O <sub>4</sub> nanotube	2 mol L <sup>-1</sup> KOH	10–38.5	5–0.20	[90]
NiCo <sub>2</sub> O <sub>4</sub> nanowire	6 mol L <sup>-1</sup> KOH	19.72–26	5–0.22	[92]
NiCo <sub>2</sub> O <sub>4</sub> nanowire	1 mol L <sup>-1</sup> KOH	15–22.6	6.9–0.22	[93]
NiCo <sub>2</sub> O <sub>4</sub> flower	6 mol L <sup>-1</sup> KOH	17.3–28.2	13.88–0.28	[95]

occurs, including forming new structures or pathways to facilitate electron and proton conduction, expanding active sites, improving cycling stability, and so on.

(3) Achieving high energy and power density simultaneously by constructing hybrid electrochemical capacitor devices. Through combining different cathodes and anodes to form an asymmetric capacitor, a higher working voltage may be produced to dramatically enhance the energy storage. For example, in a capacitor through combining a pseudocapacitive electrode with a battery-like electrode, the battery-like electrode may provide high energy density while the pseudocapacitive electrode enables high power capability. And by designing electrolytes for optimum performance in such asymmetric configurations, a high-voltage operation may be achieved without compromising stability or long-term cyclability. Finally, the search for new materials with high performance remains an important area in nickel based pseudocapacitors studies.

## Acknowledgments

This work was partially supported by Jiangsu Provincial “Qin-Lan” project, the National Natural Science Foundation of China (51175212, 51202081), the Natural Science Foundation of Jiangsu Province (BK2012244), the College Natural Science Foundation of Jiangsu Province (12KJB430003), the overseas training project of Jiangsu Province for outstanding young teachers and principals in colleges, and the US National Science Foundation EPSCoR grant (IIA-1301765).

## References

- [1] J.M. Tarascon, M. Armand, *Nature* 414 (2001) 359–367.
- [2] M. Winter, R.J. Brodd, *Chem. Rev.* 104 (2004) 4245–4269.
- [3] B.E. Conway, *Electrochemical Supercapacitors: Scientific Fundamentals and Technological Applications*, Kluwer Academic/Plenum Publishers, New York, 1999.
- [4] F. Béguin, E. Frackowiak, *Supercapacitors*, Wiley, Weinheim, 2013, pp. 131–165.
- [5] A.S. Arico, P. Bruce, B. Scrosati, J.-M. Tarascon, W.V. Schalkwijk, *Nat. Mater.* 4 (2005) 366–377.
- [6] P. Simon, Y. Gogotsi, *Nat. Mater.* 7 (2008) 845–854.
- [7] J.R. Miller, P. Simon, *Science* 321 (2008) 651–652.
- [8] C. Liu, F. Li, L.P. Ma, H.M. Cheng, *Adv. Mater.* 22 (2010) E28–E62.
- [9] S.G. Kandalkara, D.S. Dhawale, C.-K. Kima, C.D. Lokhande, *Synthetic Met.* 160 (2010) 1299–1302.
- [10] K.R. Prasad, K. Koga, N. Miura, *Chem. Mater.* 16 (2004) 1845–1847.
- [11] C. Yu, L. Zhang, J. Shi, J. Zhao, J. Gao, D. Yan, *Adv. Funct. Mater.* 18 (2008) 1544–1554.
- [12] R. Liu, S. Lee, *J. Am. Chem. Soc.* 130 (2008) 2942–2943.
- [13] H. Wang, H.S. Casalongue, Y. Liang, H. Dai, *J. Am. Chem. Soc.* 132 (2010) 7472–7477.
- [14] T. Zhu, J.S. Chen, X.W. Lou, *J. Mater. Chem.* 20 (2010) 7015–7020.
- [15] K. Naoi, S. Ishimoto, J.-I. Miyamoto, W. Naoi, *Energy Environ. Sci.* 5 (2012) 9363–9373.
- [16] D.M. Anjos, J.K. McDonough, E. Perre, G.M. Brown, S.H. Overbury, Y. Gogotsi, V. Presser, *Nano Energy* 2 (2013) 702–712.
- [17] G. Yu, X. Xie, L. Pan, Z. Bao, Y. Cui, *Nano Energy* 2 (2012) 213–234.
- [18] Q. Cai, D.J.L. Brett, D. Browning, N.P. Brandon, *J. Power Sources* 195 (2010) 6559–6569.
- [19] G. Wang, L. Zhang, J. Zhang, *Chem. Soc. Rev.* 41 (2012) 797–828.
- [20] L. Zhang, X.S. Zhao, *Chem. Soc. Rev.* 38 (2009) 2520–2531.
- [21] Q. Lu, M.W. Lattanzi, Y. Chen, X. Kou, W. Li, X. Fan, K.M. Unruh, J.G. Chen, J.Q. Xiao, *Angew. Chem. Int. Ed.* 50 (2011) 6847–6850.
- [22] Q. Lu, Y. Chen, W. Li, J.G. Chen, J.Q. Xiao, F. Jiao, *J. Mater. Chem. A* 1 (2013) 2331–2336.
- [23] L. Demarconnay, E. Raymundo-Piñero, F. Béguin, *Electrochim. Commun.* 12 (2010) 1275–1278.
- [24] A. Burke, *Electrochim. Acta* 53 (2007) 1083–1091.
- [25] Y. Hou, Y. Cheng, T. Hobson, J. Liu, *Nano Lett.* 10 (2010) 2727–2733.
- [26] S.W. Lee, J. Kim, S. Chen, P.T. Hammond, Y.S. Horn, *ACS Nano* 4 (2010) 3889–3896.
- [27] S.M. Bak, K.H. Kim, C.W. Lee, K.B. Kim, *J. Mater. Chem.* 21 (2011) 1984–1990.
- [28] H. Jiang, J. Ma, C. Li, *Adv. Mater.* 24 (2012) 4197–4202.
- [29] I.H. Kim, K.B. Kim, *J. Electrochem. Soc.* 153 (2006) A383–A389.
- [30] R. Vellacheri, V.K. Pillai, S. Kurungot, *Nanoscale* 4 (2012) 890–896.
- [31] J.W. Lang, L.B. Kong, W.J. Wu, Y.C. Luo, L. Kang, *Chem. Commun.* (2008) 4213–4215.
- [32] M.S. Wu, Y.A. Huang, J.J. Jow, W.D. Yang, C.Y. Hsieh, H.M. Tsai, *Int. J. Hydrogen Energy* 33 (2008) 2921–2926.
- [33] Y. Ren, L. Gao, *J. Am. Ceram. Soc.* 93 (2010) 3560–3564.
- [34] D.C. Wang, W.B. Ni, H. Pang, Q.Y. Lu, Z.J. Huang, J.W. Zhao, *Electrochim. Acta* 55 (2010) 6830–6835.
- [35] X.J. Zhang, W.H. Shi, J.X. Zhu, W.Y. Zhao, J. Ma, S. Mhaisalkar, T.L. Maria, Y.H. Yang, H. Zhang, H.H. Hng, Q.Y. Yan, *Nano Res.* 3 (2010) 643–652.
- [36] X.H. Xia, J.P. Tu, X.L. Wang, C.D. Gu, X.B. Zhao, *J. Mater. Chem.* 21 (2011) 671–679.
- [37] C.K. Liu, M.A. Anderson, *J. Electrochem. Soc.* 143 (1996) 124–130.
- [38] Q. Lu, J.G. Chen, J.Q. Xiao, *Angew. Chem. Int. Ed.* 52 (2013) 1882–1889.
- [39] J.P. Zheng, T.R. Jow, *J. Electrochim. Soc.* 142 (1995) L6–L8.
- [40] L. Wang, X. Liu, X. Wang, X. Yang, L. Lu, *J. Mater. Sci. Mater. Electron.* 22 (2011) 601–606.
- [41] R. Ranjusha, A.S. Nair, S. Ramakrishna, P. Anjali, K. Sujith, K.R.V. Subramanian, N. Sivakumar, T.N. Kim, S.V. Nair, A. Balakrishnan, *J. Mater. Chem.* 22 (2012) 20465–20471.
- [42] J. Li, W. Zhao, F. Huang, A. Manivannan, N. Wu, *Nanoscale* 3 (2011) 5103–5109.
- [43] Z. Lu, Z. Chang, J. Liu, X. Sun, *Nano Res.* 4 (2011) 658–665.
- [44] D. Su, H.S. Kim, W.S. Kim, G. Wang, *Chem. Eur. J.* 18 (2012) 8224–8229.
- [45] Y.Q. Zhang, X.H. Xia, J.P. Tu, Y.J. Mai, S.J. Shi, X.L. Wang, C.D. Gu, *J. Power Sources* 199 (2012) 413–417.
- [46] S. Vijayakumar, S. Nagamuthu, G. Muralidharan, *ACS Appl. Mater. Interfaces* 5 (2013) 2188–2196.
- [47] K. Liang, X. Tang, W. Hu, *J. Mater. Chem.* 22 (2012) 11062–11067.
- [48] X. Li, S. Xiong, J. Li, J. Bai, Y. Qian, *J. Mater. Chem.* 22 (2012) 14276–14283.
- [49] H. Chai, X. Chen, D. Jia, S. Bao, W. Zhou, *Mater. Res. Bull.* 47 (2012) 3947–3951.
- [50] H. Pang, Y. Shi, J. Du, Y. Ma, G. Li, J. Chen, J. Zhang, H. Zheng, B. Yuan, *Electrochim. Acta* 85 (2012) 256–262.
- [51] S.I. Kim, J.S. Lee, H.J. Ahn, H.K. Song, J.H. Jang, *ACS Appl. Mater. Interfaces* 5 (2013) 1596–1603.
- [52] Y. Hu, Y.V. Tolmachev, D.A. Scherson, *J. Electroanal. Chem.* 468 (1999) 64–69.
- [53] S. Xing, Q. Wang, Z. Ma, Y. Wu, Y. Gao, *Mater. Lett.* 78 (2012) 99–101.
- [54] D.S. Kong, J.M. Wang, H.B. Shao, J.Q. Zhang, C.N. Cao, *J. Alloy. Compd.* 509 (2011) 5611–5616.
- [55] S. Lv, H. Suo, J. Wang, Y. Wang, C. Zhao, S. Xing, *Colloid. Surf. A* 396 (2012) 292–298.
- [56] C. Yuan, X. Zhang, L. Su, B. Gao, L. Shen, *J. Mater. Chem.* 19 (2009) 5772–5777.
- [57] X. Sun, G. Wang, J.Y. Hwang, J. Lian, *J. Mater. Chem.* 21 (2011) 16581–16588.
- [58] M. Yang, J.X. Li, H.H. Li, L.W. Su, J.P. Wei, Z. Zhou, *Phys. Chem. Chem. Phys.* 14 (2012) 11048–11052.
- [59] C.Y. Cao, W. Guo, Z.M. Cui, W.G. Song, W. Cai, *J. Mater. Chem.* 21 (2011) 3204–3209.
- [60] R.J. Zou, Z.Y. Zhang, L. Yu, Q.W. Tian, Z.G. Chen, J.Q. Hu, *Chem. Eur. J.* 17 (2011) 13912–13917.
- [61] X. Huang, X.Y. Qi, F. Boey, H. Zhang, *Chem. Soc. Rev.* 41 (2012) 666–686.
- [62] Y. Jiang, D. Chen, J. Song, Z. Jiao, Q. Ma, H. Zhang, L. Cheng, B. Zhao, Y. Chu, *Electrochim. Acta* 91 (2013) 173–178.
- [63] X. Xia, J. Tu, Y. Mai, R. Chen, X. Wang, C. Gu, X. Zhao, *Chem. Eur. J.* 17 (2011) 10898–10905.
- [64] J. Yan, Z. Fan, W. Sun, G. Ning, T. Wei, Q. Zhang, R. Zhang, L. Zhi, F. Wei, *Adv. Funct. Mater.* 22 (2012) 2632–2641.
- [65] S. Chen, J. Duan, Y. Tang, S.Z. Qiao, *Chem. Eur. J.* 19 (2013) 7118–7124.
- [66] Y. Wang, S. Gai, N. Niu, F. He, P. Yang, *J. Mater. Chem. A* 1 (2013) 9083–9091.
- [67] J. Ji, L.L. Zhang, H. Ji, Y. Li, X. Zhao, X. Bai, X. Fan, F. Zhang, R.S. Ruoff, *ACS Nano* 7 (2013) 6237–6243.
- [68] Z. Tang, C. Tang, H. Gong, *Adv. Funct. Mater.* 22 (2012) 1272–1278.
- [69] D.P. Dubal, G.S. Gund, C.D. Lokhande, R. Holze, *ACS Appl. Mater. Interfaces* 5 (2013) 2446–2454.
- [70] L. Fan, L. Tang, H. Gong, Z. Yao, R. Guo, *J. Mater. Chem.* 22 (2012) 16376–16381.
- [71] S. Cheng, L. Yang, Y. Liu, W. Lin, L. Huang, D. Chen, C.P. Wong, M. Liu, *J. Mater. Chem. A* 1 (2013) 7709–7716.
- [72] M. Hasan, M. Jamal, K.M. Razeeb, *Electrochim. Acta* 60 (2012) 193–200.
- [73] J.Y. Kim, S.H. Lee, Y. Yan, J. Oh, K. Zhu, *RSC Adv.* 2 (2012) 8281–8285.
- [74] J.B. Wu, Z.G. Li, Y. Lin, *Electrochim. Acta* 56 (2011) 2116–2121.
- [75] B. Qu, L. Hu, Y. Chen, C. Li, Q. Li, Y. Wang, W. Wei, L. Chen, T. Wang, *J. Mater. Chem. A* 1 (2013) 7023–7026.
- [76] H. Pang, Y. Ma, G. Li, J. Chen, J. Zhang, H. Zheng, W. Du, *Dalton Trans.* 41 (2012) 13284–13291.
- [77] K. Xu, R. Zou, W. Li, Y. Xue, G. Song, Q. Liu, X. Liu, J. Hu, *J. Mater. Chem. A* 1 (2013) 9107–9113.
- [78] J.H. Zhong, A.L. Wang, G.R. Li, J.W. Wang, Y.N. Ou, Y.X. Tong, *J. Mater. Chem.* 22 (2012) 5656–5665.
- [79] X. Xia, J. Tu, Y. Zhang, X. Wang, C. Gu, X.B. Zhao, H.J. Fan, *ACS Nano* 6 (2012) 5531–5538.
- [80] C. Guan, X. Li, Z. Wang, X. Cao, C. Soci, H. Zhang, H.J. Fan, *Adv. Mater.* 24 (2012) 4186–4190.

[81] L. Jiang, R. Zou, W. Li, J. Sun, X. Hu, Y. Xue, G. He, J. Hu, *J. Mater. Chem. A* 1 (2013) 478–481.

[82] F. Yang, J. Yao, F. Liu, H. He, M. Zhou, P. Xiao, Y. Zhang, *J. Mater. Chem. A* 1 (2013) 594–601.

[83] X. Wang, A. Sumboja, M. Lin, J. Yan, P.S. Lee, *Nanoscale* 4 (2012) 7266–7272.

[84] Y.F. Yuan, X.H. Xia, J.B. Wu, J.L. Yang, Y.B. Chen, S.Y. Guo, *Electrochim. Acta* 56 (2011) 2627–2632.

[85] M. Jin, G. Zhang, F. Yu, W. Li, W. Lu, H. Huang, *Phys. Chem. Chem. Phys.* 15 (2013) 1601–1605.

[86] K. Liang, N. Wang, M. Zhou, Z. Cao, T. Gu, Q. Zhang, X. Tang, W. Hu, B. Wei, *J. Mater. Chem. A* 1 (2013) 9730–9736.

[87] C. Yuan, J. Li, L. Hou, X. Zhang, L. Shen, X.W. Lou, *Adv. Funct. Mater.* 22 (2012) 4592–4597.

[88] G.Q. Zhang, H.B. Wu, H.E. Hoster, M.B. Chan-Park, X.W. Lou, *Energy Environ. Sci.* 5 (2012) 9453–9456.

[89] G. Zhang, X.W. Lou, *Adv. Mater.* 25 (2013) 976–979.

[90] L. Li, S. Peng, Y. Cheah, P. Teh, J. Wang, G. Wee, Y. Ko, C. Wong, M. Srinivasan, *Chem. Eur. J.* 19 (2013) 5892–5898.

[91] R. Zou, K. Xu, T. Wang, G. He, Q. Liu, X. Liu, Z. Zhang, J. Hu, *J. Mater. Chem. A* 1 (2013) 8560–8566.

[92] H. Wang, Q. Gao, L. Jiang, *Small* 7 (2011) 2454–2459.

[93] H. Jiang, J. Ma, C. Li, *Chem. Commun.* 48 (2012) 4465–4467.

[94] T.Y. Wei, C.H. Chen, H.C. Chien, S.Y. Lu, C.C. Hu, *Adv. Mater.* 22 (2010) 347–351.

[95] H. Chen, J. Jiang, L. Zhang, T. Qi, D. Xia, H. Wan, *J. Power Sources* 248 (2014) 28–36.

[96] Y. Lei, J. Li, Y. Wang, L. Gu, Y. Chang, H. Yuan, D. Xiao, *ACS Appl. Mater. Interfaces* 6 (2014) 1773–1780.

[97] Y. Zhang, M. Ma, J. Yang, H. Su, W. Huang, X. Dong, *Nanoscale* 6 (2014) 4303–4308.

[98] X.F. Lu, D.J. Wu, R.Z. Li, Q. Li, S.H. Ye, Y.X. Tong, G.R. Li, *J. Mater. Chem. A* 2 (2014) 4706–4713.

[99] Q. Wang, X. Wang, B. Liu, G. Yu, X. Hou, D. Chen, G. Shen, *J. Mater. Chem. A* 1 (2013) 2468–2473.

[100] J. Xiao, S. Yang, *J. Mater. Chem.* 22 (2012) 12253–12262.

[101] X. Wang, X. Han, M. Lim, N. Singh, C.L. Gan, M. Jan, P.S. Lee, *J. Phys. Chem. C.* 116 (2012) 12448–12454.

[102] H.C. Chien, W.Y. Cheng, Y.H. Wang, S.Y. Lu, *Adv. Funct. Mater.* 22 (2012) 5038–5043.

[103] H. Wang, X. Wang, *ACS Appl. Mater. Interfaces* 5 (2013) 6255–6260.

[104] F. Deng, L. Yu, G. Cheng, T. Lin, M. Sun, F. Ye, Y. Li, *J. Power Sources* 251 (2014) 202–207.

[105] N. Padmanathan, S. Selladurai, *RSC Adv.* 4 (2014) 8341–8349.

[106] W. Liu, C. Lu, K. Liang, B.K. Tay, *J. Mater. Chem. A* 2 (2014) 5100–5107.

[107] W. Yang, Z. Gao, J. Ma, X. Zhang, J. Wang, J. Liu, *J. Mater. Chem. A* 2 (2014) 1448–1457.

[108] K. Xu, W. Li, Q. Liu, B. Li, X. Liu, L. An, Z. Chen, R. Zou, J. Hu, *J. Mater. Chem. A* 2 (2014) 4795–4802.

[109] L. Hou, C. Yuan, D. Li, L. Yang, L. Shen, F. Zhang, X. Zhang, *Electrochim. Acta* 56 (2011) 7454–7459.

[110] T. Zhu, Z. Wang, S. Ding, J. Chen, X.W. Lou, *RSC Adv.* 1 (2011) 397–400.

[111] J. Yang, X. Duan, Q. Qin, We Zheng, *J. Mater. Chem. A* 1 (2013) 7880–7884.

[112] S.W. Chou, J.Y. Lin, *J. Electrochem. Soc.* 160 (2013) D178–D182.

[113] J.P. Liu, C.W. Cheng, W.W. Zhou, H.X. Li, H.J. Fan, *Chem. Commun.* 47 (2011) 3436–3438.

[114] L.B. Kong, L. Deng, X.M. Li, M.C. Liu, Y.C. Luo, L. Kang, *Mater. Res. Bull.* 47 (2012) 1641–1647.

[115] W. Zhu, Z. Lu, G. Zhang, X. Lei, Z. Chang, J. Liu, X. Sun, *J. Mater. Chem. A* 1 (2013) 8327–8331.